GRACE-based dynamic assessment of hydrological drought trigger thresholds induced by meteorological drought and possible driving mechanisms

Zhiming Han[a], Shengzhi Huang[b]*, Jian Peng[cd], Jianfeng Li[e], Guoyong Leng[f], Qiang Huang[b], Jing Zhao[b], Fang Yang[g], Panxing He[h], Xiaoyu Meng[i], Zhi Li[a]*

[a] State Key Laboratory of Soil Erosion and Dryland Farming on the Loess Plateau, College of Natural Resources and Environment, Northwest A&F University, Yangling, Shaanxi 712100, China

[b] State Key Laboratory of Eco-Hydraulic in Northwest Arid Region of China, Xi'an University of Technology, Xi'an, 710048, China

[c] Department of Remote Sensing, Helmholtz Centre for Environmental Research-UFZ, Permoserstrasse 15, 04318 Leipzig, Germany

[d] Remote Sensing Centre for Earth System Research, Leipzig University, 04103 Leipzig, Germany

[e] Department of Geography and The Centre for Geo-computation Studies, Hong Kong Baptist University, Hong Kong, China

[f] Key Laboratory of Water Cycle and Related Land Surface Processes, Institute of Geographic Sciences and Natural Resources Research, Chinese Academy of Sciences, Beijing 100101, China

[g] Chinese Research Academy of Environmental Science, Beijing,100012, China

[h] Henan Normal University, Xinxiang 453007, China

[i] Key Research Institute of Yellow River Civilization and Sustainable Development & Collaborative Innovation Center on Yellow River Civilization of Henan Province, Henan University, Kaifeng 475000, China

* Correspondence: Shengzhi Huang. E-mail: huangshengzhi7788@126.com

Zhi Li. E-mail: lizhibox@126.com.

Abstract: Determining the threshold at which meteorological drought triggers hydrological drought is critical for early warning and proper mitigation of drought. However, drought trigger thresholds are difficult to determine owing to the nonlinearity between meteorological and hydrological drought, and their dynamics have not been explored. To this end, we introduce a precipitation-driven drought trigger threshold framework. This framework considers the multiscale characteristics of cumulative precipitation anomalies and incorporates the drought severity index of terrestrial water storage anomalies to characterize hydrological drought. The dynamics of trigger thresholds over time and the main drivers of these variations are further explored over China. The results show that hydrological drought is more sensitive to meteorological drought in south China, with some regions showing weak or negative correlations mainly determined by the differences between climate change and human activities. The risk of drought outbreak in the central, northeastern and southern regions of China is high, with trigger thresholds showing a dynamic decreasing trend over time (corresponding to lower cumulative precipitation anomalies), indicating weakened resistance to meteorological drought. Rising temperature is the main factor affecting dynamic changes in the trigger threshold. The drought trigger threshold framework proposed in this study is also applicable for assessments in other regions around the world. This study provides valuable insights and new approaches for understanding the mechanisms of hydrological drought formation. Furthermore, these results are expected to severe as a scientific basis for government departments to reduce water supply stress on human and natural systems and to develop adaptive

management strategies.

Key words: GRACE; cumulative precipitation anomaly; drought; trigger threshold

1 Introduction

The considerable inter-annual fluctuations in precipitation owing to changes in East Asian monsoon climate, combined with sensitive ecosystems and intensive human activities, have resulted in frequent drought events in China (Li et al., 2012). Drought begins during periods of precipitation deficit and subsequently spreads through the terrestrial hydrological system (Van Loon et al., 2012; Herrera-Estrada et al., 2017; Miao et al., 2022). Owing to the effects of climate change, water scarcity has become one of the most pressing issues in China (Zhang et al., 2014). Therefore, predicting the drought occurrence probability and corresponding precipitation deficit state in advance would be extremely beneficial for water resource management. This will improve early drought monitoring and warning and play a critical role in assisting policymakers and governmental agencies to develop adaptive management strategies.

Drought is defined in different ways, and therefore, drought cannot be characterized by a single index since existing drought indicators are associated with specific types of droughts (Svoboda et al., 2002; Azmi et al., 2016). More importantly, most existing indicators do not consider human water use and/or local water storage (Lloyd-Hughes, 2014), and thus ignore the impact of human activities on drought. For example, rainfall in northwest India increased from 2002 to 2015 and soil moisture was relatively stable. However, severe droughts still occurred owing to inadequate water storage resulting from groundwater extraction for irrigation (Sinha et al., 2017).

Although these indicators can be constructed by coupling more climate-human water-related variables (e.g., drought caused by anthropogenic factors such as urbanization, surface water and groundwater overdraft) to multivariate indices to capture drought, this remains a considerable challenge.

Drought is a complex phenomenon involving a wide range of processes spanning the atmosphere, hydrosphere, lithosphere and biosphere; most notably, it is influenced by the lower-than-historical-average level of terrestrial water storage (TWS) (Pokhrel et al., 2021). Global terrestrial water storage anomalies (TWSA) have been monitored by the Gravity Recovery and Climate Experiment (GRACE) mission with an unprecedented accuracy since 2002 (Li et al., 2021). TWSA refers to anomalies in water storage of Earth's land area in the vertical direction, including anomalies in ice and snow, surface water, soil water and groundwater. Hence, the TWSA can reflect the combined effects of climate change and human activities on watershed droughts (Famiglietti and Rodell, 2013; Long et al., 2014). For instance, many studies (Zhao et al., 2017; Sinha et al., 2019; Cui et al., 2021) have used TWSA to capture the process of drought and combined it with traditional drought indices to compensate for the lack of drought characterization by a single index, providing crucial insights for understanding the impact of drought on hydrological systems.

To the best of our knowledge, there have been relatively few studies involving drought thresholds, with most of these studies utilizing copula functions (Liu et al., 2013; Wu et al., 2021; Guo et al., 2023). This is because copula functions can be used to construct joint distribution functions for multiple variables, providing the ability to calculate conditional probabilities under different drought scenarios. For example, Guo (2020) explored the meteorological drought thresholds that trigger various levels of hydrological drought in the Weihe River basin based on the coupled standardized precipitation index (SPI) and standardized runoff index (SRI). However, their study only used a 1-month SPI and SRI match, ignoring the more severe hydrological droughts caused by long-duration precipitation deficits, which are especially common in major drought events that have occurred in the past, such as the droughts in California (Prugh et al., 2018), Australia (King et al., 2020), and southwest China (Li et al., 2021). Han (2021a) proposed a model to establish a threshold between meteorological and groundwater drought in the Xijiang River Basin. These studies have uncovered new insights and improved our understanding of drought thresholds. However, uncertainties exist in the density estimation of certain parameters used to fit the marginal distributions.

Copula functions have also been used to assess changes in food and vegetation under drought stress. Leng and Jim (2019) applied a probabilistic modelling framework constructed using copula functions to study global food production losses under drought stress. Fang et al. (2019) used copula functions to assess the spatiotemporal patterns of vegetation vulnerability in the Loess Plateau under multiple drought scenarios. While these studies have provided valuable insights into the potential impacts of droughts, they are based on traditional standardized drought indices (e.g., SPI and SPEI), which may not be directly linked to precipitation records (Santos et al., 2013), especially in data-scarce regions. This is because the calculation of standardized indices requires long-term precipitation data (Vicente-Serrano et al., 2010). The construction of standardized indices also often requires the fitting of specific distribution functions, and may require data on temperature, evapotranspiration, soil moisture and other parameters, in addition to precipitation data. This poses significant challenges for the implementation of drought early warning and prevention measures at local levels. Conversely, compared with the abstract thresholds typically associated with standardized values, thresholds corresponding to precipitation can be directly related to different sectors or regions. This also provides key scientific guidance for governments to coordinate adaptation/mitigation strategies among different sectors/regions. More crucially, the forementioned studies have failed to account for the fact that the thresholds are not fixed. Rather, trigger thresholds are subject to dynamic changes, because climate change influences the hydrological cycle and complicates the link between precipitation and TWS. Furthermore, the drivers of these differences are still unclear.

This study takes into account the multi-scale features of the cumulative precipitation anomalies (CPA), employs the drought severity index of terrestrial water storage anomalies (TWSA-DSI) to characterize hydrological drought, and presents a novel precipitation-driven drought trigger threshold model. The primary objectives of this study are to (1) reveal the threshold and dynamic changes in precipitation triggered drought; and (2) explore the main factors affecting the threshold. The results of this study will not only help monitor and predict droughts more accurately, but are also expected to complement direct evidence of intensified water cycles.

2 Data and methods

2.1 Study area

China's terrain is high in the west and low in the east, with mountains, plateaus and hills covering approximately 67% of its land area, and basins and plains covering approximately 33% of its land area (Jin et al., 2021). China spans a wide range of latitudes and longitudes, with considerable variations in the combinations of temperature and precipitation, creating a wide variety of climates. The eastern part of China has a monsoon climate, the northwestern part has a temperate continental arid climate, and the Tibetan Plateau has an alpine climate. China is characterized by a monsoon climate with warm rainy summers and dry cold winters. Although the variety in climate types in China is favorable for agricultural production, extreme climate events, such as droughts, floods, cold waves, and typhoons, have considerable impacts on the country. Based on the classification of Chinese watershed systems, we considered nine major river basins (Fig. 1), namely the Songliao River Basin (Ⅰ), Hai River Basin (Ⅱ), Huai River Basin (Ⅲ), Southeast River Basin (Ⅳ), Pearl River Basin (Ⅴ), Yellow River Basin (Ⅵ), Yangtze River Basin (Ⅶ), Southwestern River Basin (Ⅷ) and Inland River Basin (Ⅸ).

Fig. 1 Location map of the study area.

2.2 Datasets

2.2.1 GRACE data

The TWSA were obtained from the GRACE RL06 mascon product of the University of Texas Center for Space Research (CSR) for the periods January 2004-July 2017, and May 2018-December 2019 with a spatial resolution of 0.25° (obtained from http://www2.csr.utexas.edu/grace/RL06.html). Regarding the approximately one-year interval between the GRACE and GRACE-Follow-On for the observation of TWSA, many scholars have conducted reconstruction and interpolation (Sun et al., 2019; Sun et al., 2020; Mo et al., 2021). To better match with CSR products, here we use the data from Zhong et al (2020). Besides, we use the mascon products from the National Aeronautics and Space Administration Goddard Space Flight Center (GSFC) and the Jet Propulsion Laboratory (JPL). The interpolated data was obtained separately using the reconstructed data from Li et al (2021).

2.2.2 Hydrometeorological data

Gridded precipitation and air temperature data were obtained from the China Meteorological Data Service Center (http://data.cma.cn). In this dataset, gridded monthly precipitation data from 1999-2019 was generated by a thin plate spline spatial interpolation of precipitation observations from 2,472 weather stations, and the spatial resolution is 0.5° (Hong et al., 2005). As no data are available for Taiwan, the study focuses on mainland China. Moreover, the nearest neighbor method was used to resample precipitation data into 0.25° grid for better comparison with CSR products. The evaporation flux from soil used version 2.1/Noah land surface model products from the Global Land Data Assimilation System (GLDAS) with 0.25° spatial resolution and monthly temporal resolution (http://disc.sci.gsfc.nasa.gov). The vapor pressure deficit (VPD) was derived from the TerraClimate dataset and has the same spatial and temporal resolutions as other products (http://www.climatologylab.org/terraclimate.html).

2.2.3 Vegetation data

The normalized vegetation index (NDVI) can effectively reflect the vegetation parameters such as vegetation coverage, growth status, biomass and net primary productivity (Fensholt et al., 2012). In this study, the 2003-2019 NDVI dataset from the Moderate Resolution Imaging Spectroradiometer (MODIS) of NASA's MOD13C2 product was selected. Its spatial resolution is 0.05° and its temporal resolution is month (https://modis.gsfc.nasa.gov/data/)., and it was resampled to 0.25° resolution in this study.

2.2.4 Population and economic data

Population data for China were obtained from WorldPop on the annual scale with a spatial resolution of 1km (https://www.worldpop.org/). For comparison with other data, the 1km population data were counted to a 0.25° grid. The Gross Domestic Product (GDP) data are derived from the global-scale, high-precision products of Chen et al (2022). This product is calculated from nighttime lights data using a series of methods, such as Particle Swarm Optimization-Backpropagation (PSO-BP) algorithm.

3 Methods

3.1 Cumulative precipitation anomalies

Compared with SPI, CPA can provide the most direct reference for early warning of meteorological and risk management (Van den Broeke et al., 2009; Coelho et al., 2016). In order to describe the precipitation deficit corresponding to hydrological drought, the cumulative precipitation deficit series with climatological significance at different time scales were established:

$$CPA_t = \sum_{i=1}^{t} (P_t - \overline{P_m}) \tag{1}$$

where P_t is the precipitation in period t; and $\overline{P_m}$ represents the average precipitation of the cumulative months in the same period.

3.2 Drought severity index of terrestrial water storage anomaly

TWSA-DSI was defined as the standardized anomalies of TWSA values, as follows:

$$TWSA - DSI_{i,j} = \frac{TWSA_{i,j} - \overline{TWSA_j}}{\sigma_j} \tag{2}$$

where i is year ranging from 2003 to 2019; j is month ranging from January to December; $\overline{TWSA}$ and σ_j are the mean and standard deviation of TWSA in month j, respectively (Zhao et al., 2017).

3.3 Population-GDP index

Population-GDP index (PGI) is an index constructed based on the exposure characteristics emphasized by Intergovernmental Panel on Climate Change (IPCC) and the United Nations International Strategy for Disaster Reduction and fully considering the factors of population and economic development (Field et al., 2012).

$$PGI_n^m = (1/2)^{\ln(9+POP_{\max}^m / POP_n^m)} + (1/2)^{\ln(9+GDP_{\max}^m / GDP_n^m)} \tag{3}$$

where POP_n^m and GDP_n^m are the population and GDP values corresponding to pixel m in year n, respectively; $POP_{\max}^m$ and $GDP_{\max}^m$ are the maximum values of population and

GDP in China at year m on the metric scale, respectively

3.4 Probabilistic framework for trigger threshold

Copula functions (Eq. 4) provide the flexibility to represent a multivariate joint distribution, which is not limited by the marginal distribution of random variables or the type of joint distribution function, thus avoiding assumptions about linearity or underlying probability distributions (Nelsen, 2007). In this study, the CPA at the best scale (the CPA values at 1-24 month scales were compared separately) matched by the DSI in each grid was identified using Spearman maximum correlation coefficient ($p<0.05$). Parametric distributions have limited efficiency because of the uncertainties in parameter estimation, and are invalid for random variables less than zero (Peter D, 1985). The kernel distribution (Eq. 5) was thus employed to fit them to the marginal distribution, and then the copula function was used to construct the joint probability distribution between CPA (x) and TWSA-DSI (y).

$$F_{XY}(X,Y) = C[F_X(X), F_Y(Y)] \tag{4}$$

where $F_X(X)$ and $F_Y(Y)$ are the marginal distributions of x and y, respectively. C is the cumulative distribution function of copula.

For any real values of x, the probability density function of the kernel density estimator's formula was given by:

$$\widehat{f_h}(x) = \frac{1}{nh}\sum_{i=1}^{n} K\left(\frac{x-x_i}{h}\right) \tag{5}$$

where x_1, x_2, … x_n are random samples from an unknown distribution, n is the sample size, K is the kernel smoothing function, and h represents the bandwidth (Wang et al., 2021).

There are five commonly used bivariate copula functions in current practice, denoted as Clayton, Gumbel, Frank, t, and Gaussian. Among these, the Frank, Clayton and Gumbel copulas are Archimedes-type copulas, which have been widely used in the analysis of extreme hydrological events (Santhosh and Srinivas, 2013; Sadegh et al., 2017). Different copulas have different tail dependences: the Clayton and Gumbel copulas have lower and upper tail dependences, respectively, whereas the Frank copula has no tail dependence (Guo et al., 2021). For the drought scenario, we focused more on the probability that the TWSA-DSI decreases as the CPA decreases (lower tail dependence).

Fig. 2 depicts the comparison between the observed combination of CPA and TWSA-DSI and the simulation of random variables using the Clayton copula function. The consistency pattern of the simulated and empirical copula shows that the proposed model performs well in modelling the dependence between CPA and TWSA-DSI. Besides, Fig. 2 shows that Clayton copula has lower tail dependence, which is the concern of this study. The percentiles were used in this study to define the different levels of CPA and TWSA-DSI, with values in the 40^{th}-30^{th}, 30^{th}-20^{th}, 20^{th}-10^{th} and, $\leq 10^{th}$ percentile ranges corresponding to mild, moderate, severe, and extreme levels of drought. The conditional probabilities of occurrence of different levels of drought ($Y \leq y$) under scenarios with different levels of precipitation deficit ($x_2 < X \leq x_1$) can be expressed as follows:

$$P(Y \leq y | x_2 < X \leq x_1) = \frac{P(x_2 < X \leq x_1, Y \leq y)}{P(x_2 < X \leq x_1)} \tag{6}$$

Further, for a given level of drought, the probability of drought occurrence will theoretically converge to 1 as the precipitation anomaly continues to exhibit a deficit.

In the probabilistic framework represented in Fig. 3, the percentile of CPA is iteratively adjusted from the 50th to the 1st percentile, signifying a progressive rise in precipitation deficit. This iterative process enables the estimation of the conditional probability associated with each iteration, thereby indicating possible scenarios leading to hydrological drought under the corresponding conditional probability. The configuration of the conditional probabilities can be flexible and variable depending on the requirements of the decision maker and the local climatic conditions. The conditional probability was fixed at 0.5 in this study, indicating that if the conditional probability was equal to or greater than 0.5, there would be a 50% chance that the CPA state at that percentile would lead to a hydrological drought. Consequently, the corresponding CPA value at that level was identified as the threshold for triggering drought conditions. Conversely, if the conditional probability remained below 0.5 as the CPA was progressively increased to the 1st percentile, it was presumed that there was no trigger threshold associated with that particular pixel. Moreover, based on the Clayton copula, the conditional probability density distribution (PDF) of $f_{Y|X}(y|x)$ was derived as follows:

$$f_{Y|X}(y \mid x) = c[F_X(X), F_Y(Y)] \cdot f_Y(y) \tag{7}$$

where c is the copula, $f_Y(y)$ is the PDF of TWSA-DSI. Once we choose a certain CPA conditional PDF from Eq. 6, the probability of TWSA-DSI (Y) dropping below a particular threshold (y) is given by the area under the curve $f_{Y|X}(y|x)$.

Fig. 2 The comparison between the observed combination of CPA and TWSA-DSI and the simulation of random variables using the Clayton copula function. The r_s and r_e are the correlation coefficient of simulations and observations, respectively. Note: "**" represents significance level of 0.01.

Fig. 3 Precipitation-driven drought trigger threshold framework.

3.5 The random forest method

The random forest (RF) method introduces the Bagging idea, randomly and independently extracts the sub-sample set, and independently constructs the decision tree for calculation (Quinlan, 1986; Breiman, 2011). When constructing the decision tree, each node randomly selects the feature subset, from which the optimal feature is selected for splitting (Cai et la., 2019). These make the model have better prediction ability, good tolerance to noise and outliers, and avoid overfitting to some extent. In this study, RF was used to explore the relative contribution of each factor to the trigger threshold and identify the main driving factors. The number of decision trees and the number of leaf nodes in the subtrees were 100 and 2 respectively.

4 Results

4.1 Dependence of TWSA-DSI on CPA

Considering that TWSA-DSI is an integrated characterization of the drought signal, it may contain both short-term and long-term scales of response to precipitation. To select the best response time, the Spearman correlation coefficients between CPA and TWSA-DSI were calculated on 1-24 month scales, and the scale corresponding to the largest correlation in each pixel was identified. Fig. 4a demonstrates that the correlation between CPA and TWSA-DSI ranged from -0.25 to 0.89, with approximately 81% of the pixels passing the 95% significance test. It is worth noting that the correlation tends to be higher in humid and subhumid areas with abundant precipitation, e.g., the Pearl River Basin, Southeast River Basin and Songhua River Basin. In contrast, the correlation tends to be lower in arid and semi-arid areas, e.g., inland river basins and the central part of the Yellow River Basin. Typically, the TWSA is directly affected by precipitation and shows higher consistency in areas with abundant precipitation. However, TWSA is also influenced by glacial snowmelt, evapotranspiration and human activities (Scanlon et al., 2018; Li et al., 2018). Many studies (Feng et al., 2016; Jin et al., 2018; Zhao et al., 2021) have shown that since the implementation of the ecological restoration project in 1999, the rapid increase in vegetation cover in the Loess Plateau is likely to be one of the main factors leading to the decline in TWSA, while precipitation shows a slight upward trend during this period (Han et al., 2021b). The central part of the Yellow River Basin and the Hai River Basin are affected by groundwater overdraft and exhibit a long-term deficit of water reserves, thus showing a negative correlation. In addition, the negative correlation exhibited in the Southwestern River Basin (Ⅷ) is mainly related to the reduction in glacial snowmelt.

The significant positive correlation between TWSA-DSI and CPA in this study is the premise of constructing copula function. The pixels with positive correlation coefficients at the 95% significance level were selected and further matched to the corresponding optimal scale, i.e., response time (Fig. 4b). The response time of TWSA-DSI increases gradually from humid to arid areas. This was because TWSA includes surface water (reservoir storage and lake), soil water and groundwater components, and there exist significant differences in the weight of these components in different regions. For instance, in humid areas, surface water and soil water show a greater proportion of TWSA as well as a shorter response time to precipitation, while in the arid and semi-arid areas, soil water and groundwater show a greater proportion and a longer response time to precipitation.

Fig. 4 Correlation between drought and precipitation (a) and its response time (b). The white pixels in b indicate the failure to pass the test for significant ($p<0.05$) positive correlation.

4.2 Probability of triggering drought under various CPA scenarios

Given the complexity and randomness of drought risk, we provide comprehensive estimates of different combinations of droughts that trigger each of the four classes of hydrological drought under corresponding CPA scenarios (Fig. 5). The risk of drought in central, southeast, and northeast China was clearly observed to be high, especially in the Pearl River Basin and the Songhua River Basin, which are areas at high risk of extreme drought. This is consistent with the five distinct drought centers in China during the recent 50 years, including the northeast region, Huang

Huai Hai region (eastern part of Northwest China and North China), Yangtze River Basin, South China and Southwest China (Ma et al., 2018; Yu and Zhai, 2021). For a certain level of drought (along each column), the probability of causing the same degree of drought and the area affected gradually increased as the CPA percentile gradient decreased. Similarly, under a certain level of CPA stress (along each row), the probability and area of drought tended to decrease as drought events progressed from mild to extreme. These significant spatial differences were not only consistent with actual conditions, but also provided direct evidence for identifying areas prone to drought.

Notably, humid areas with high amounts of precipitation tend to exhibit a higher risk of drought than arid and semi-arid areas with low amounts of precipitation and dry climates. Precipitation in China mainly occurs during June-September due to obvious geographical differences in precipitation distribution and the influence of the warm and humid monsoon. Although the annual precipitation in arid and semi-arid areas is lower than that in humid areas, the intra-annual variability in precipitation is lower than that in humid areas. In contrast, the greater dependence of TWSA on precipitation in humid areas further suggested that the persistent deficit of precipitation was the main factor leading to drought.

Fig. 5 Probability of triggering different levels (mild, moderate, severe and extreme) of drought under different percentile precipitation scenarios. The different CPA and TWSA-DSI scenarios are represented by the X and Y in the panel.

4.3 Trigger thresholds corresponding to different levels of drought

Prior knowledge of what level of CPA is likely to trigger what level of drought facilitates better prediction and early warning of drought occurrences. Fig. 6 shows the CPA corresponding to different levels of drought. The color within each pixel indicates the CPA corresponding to the occurrence of that level of drought. When equal to or below this value, there is at least a 0.5 probability of triggering the occurrence of drought. A darker color in the pixel indicates a higher trigger threshold, i.e., a higher CPA is required. Furthermore, comparison with Fig. 4b reveals that the pixels of the trigger threshold were significantly reduced as the drought level increased. Despite coupling two indices of optimal scale, the conditional probability of these pixels may not reach 0.5 when precipitation is not the primary control. Moreover, with increasing drought levels, the required CPA is lower (lower limit is the 1st percentile), and there may be no corresponding trigger thresholds. It is further shown that there are factors other than precipitation that influence drought occurrence. The CPA exhibits higher values in the southern region of China under all scenarios, while the response time in the northwest is comparatively longer. However, the CPA in the northwest may not reach the same magnitude as the 1-month deficit observed in the south. This discrepancy can be attributed to significant variations in average annual precipitation among different climatic zones.

To clearly compare the resistance of TWS to precipitation deficits between pixels, Fig. 7 shows the percentile differences in CPA corresponding to mild drought. The high value areas are concentrated in the northeastern, central and southern regions, indicating that these regions are less resistant, and more prone to drought. In the trigger thresholds of mild grade drought, the percentage of CPA pixels in mild, moderate, severe, and extreme grades are 0.3%, 30.1%, 38.3%, and 31.3%, respectively. This shows that the severe grade is the main grade of CPA that induces drought in China. Furthermore, for extreme hydrological droughts, close to 100% of like elements are required to achieve extreme levels of CPA, which means that extreme CPA scenarios require even more attention and action from the relevant authorities. This also indicates that if we can estimate and ascertain the required the CPA based on response time, we can proactively forecast and understand the risk probability of potential drought events of different severity levels.

Fig. 6 CPA corresponding to different levels of drought trigger thresholds. The white pixels in the panel indicate no threshold, and the same applies to subsequent figures.

Fig. 7 CPA percentiles corresponding to different levels of drought trigger thresholds.

4.4 Dynamic evolution of trigger thresholds

To better analyze the dynamic evolution characteristics of triggering thresholds under changing environmental conditions, the time series data was divided into 11, 9, and 7 sub-sequences using sliding windows of 7, 9, and 11 years, respectively, with a sliding step of 1 year. Next, each subsequence was brought into the threshold framework, and threshold results in the same pixel in all periods were filtered, and the trend of thresholds was analyzed using the Sen's slope and the Mann-Kendall trend test. As the level of meteorological drought increased, the number of pixels filtered at the same position was evidently reduced. To more comprehensively capture the dynamic evolution of trigger thresholds at the national scale, only the results of mild drought are shown herein. Fig. 8 shows the trend of CPA changes corresponding to triggering mild drought at the pixel scale. Under the sliding windows of 11, 9, and 7 years, 70%, 68%, and 69% of the pixels showed a decreasing trend, respectively, indicating that the cumulative precipitation deficit corresponding to the triggering threshold was decreasing. This further suggested that the resilience of drought to meteorological stress was decreasing. At the basin scale, the Pearl River Basin and the lower reaches of the Yangtze River Basin exhibited a significant ($p<0.05$) downward trend. Related studies (Sun et al., 2012; Chen et al., 2015) have shown that the frequency of droughts in southern China has increased significantly since the beginning of the 21st century, and the increase in seasonal drought events has been particularly pronounced. Huang et al. (2018) found that the southeastern part of the Yangtze River Basin has exhibited drought conditions since 2000. Therefore, our study characterizes in detail the spatio-temporal dynamic evolution characteristics of the trigger threshold, which further indicates that drought risk management in these regions faces considerable challenges.

Fig. 8 Spatial trends in thresholds corresponding to mild drought under sliding windows of 11 (a), 9 (b), and 7 years (c), with black markers indicating significance at the 0.05 level. Histograms in panels show statistical proportions.

4.5 Primary factors affecting dynamic changes in trigger thresholds

The dynamic changes in the trigger threshold reflect the integrated response of regional water resource systems to meteorological drought stress under environmental change. To investigate the controls of propagation thresholds, the same sliding window was used for air temperature (T), evaporation flux from soil (ES), NDVI, VPD, and PGI, and the contributions of the driving factors were identified using random forest regression. Considering the variable magnitudes and large spatial heterogeneity of the controlling factors, differences between the mean value of each factor and the trigger thresholds are discussed here. Considering that the factors used in the analysis of driving forces were derived from different datasets and there may have been severe collinearity among them, we used the Variance Inflation Factor (VIF) to diagnose the severity of multicollinearity among the factors. A VIF value of 10 is commonly used as an empirical threshold to assess the severity of multicollinearity among predictor variables, with values greater than 10 indicating severe multicollinearity (Stine, 1995). There was no covariance among the factors, except that the VIF of PGI and T approached 10 (Fig. S1). The GDP data used in this study were derived from nighttime light data (Chen et al., 2022), which were known to be influenced by temperature changes. In particular, from the perspective of China's electricity demand structure, an increase in both cooling and warming days would significantly increase electricity consumption in urban and rural residential areas (Yang, 2019). Meanwhile, to ensure the reliability of the methodology, the model prediction results for each time period were evaluated using Nash-Sutcliffe efficiency (NSE) and correlation coefficient (r).

Changes in the relative importance scores of various factors under different sliding windows show similar trends. However, over the whole period, temperature emerged as the most important factor influencing the dynamic changes in the trigger threshold (Fig. 9). During periods of precipitation deficit, the TWS may be further depleted due to a lack of replenishment, and changes in high temperatures may exacerbate water consumption, resulting in a lower trigger threshold and an increase in the occurrence of drought events. For example, during the late 20^{th} century and the beginning of the 21^{st} century, the southern states of the United States of America experienced a pronounced warming trend, which was attributed to synchronous changes in water vapor pressure and relative humidity. The intensification of temperature changes is predicted to result in more frequent extreme events in the future (Chiang et al., 2018). Further direct evidence suggests that while meteorological drought was the main driving factor for the hot-dry events in the 1930s, the primary driving factor in recent decades has become the observed warming trend (Alizadeh et al., 2020). Dry soils contribute to temperature rise, heat advection and atmospheric boundary layer deepening. The latter, in turn, increases evaporation demand, further drying the soil and raising temperatures. This drying and warming cycle suppresses cloud formation, inhibits local convective precipitation, and exacerbates drought conditions (Schumacher et al., 2019). Moreover, climate warming has been shown to exacerbate the duration and intensity of droughts in China, meaning that more water may be lost, reducing the water available for groundwater recharge (Chen et al., 2015; Gu et al., 2020; Jiang et al., 2022). As soil water and groundwater are the main important components of the TWS, the intensification of climate change indirectly affects the dynamics of the trigger threshold while accelerating water cycle processes.

Fig. 9 Relative importance of various factors on triggering thresholds under sliding windows of 11 (a), 9 (b), and 7 years (c). Note: PGI, VPD, T, ES, NDVI, r and NSE represent population-GDP index, vapor pressure deficit, air temperature, evaporation flux from soil, normalized vegetation index, correlation coefficient and Nash-Sutcliffe efficiency respectively.

----

5 Discussion

5.1 Validation of other results from other GRACE products

We used GSFC and JPL products to further assess the robustness of the results. The spatial correlations of GSFC and JPL with CPA show similar changes (Fig. S2a, b), and are highly consistent with the results from CSR. Compared to the correlations, the response times of the three products to CPA were slightly different (Fig. S2c, d), and these differences may be related to the calculation methods used for each product

(Long et al., 2017; Chen et al., 2021). We further entered the GSFC and JPL products into the probabilistic framework and calculated the corresponding CPA changes leading to the mild and extreme drought scenarios (Fig. S3). Both scenarios showed a spatially effective distribution of pixels and chromaticity changes that were consistent with the CSR product. In addition, we resampled the threshold results to a resolution of 0.25° for a more direct comparison with the CSR results (Fig. 10). We found that the absolute changes primarily ranged between -10 mm and 50 mm (Fig. 10a, b, c, d: 94%, 93%, 84%, 80% respectively). The main differences in precipitation were concentrated in the wetter southern regions and were significantly larger for extreme droughts than for mild droughts (Fig. 10c, d). This is indeed the case, as extreme levels of CPA are required to trigger extreme droughts. These differences may also be influenced by the correlation between CPA and TWSA-DSI, as well as the fitting process of the joint distribution function within the threshold framework.

We assessed the reliability of the CSR results from a dynamic perspective. Fig. 11 shows the changes in the sliding threshold of the GSFC and JPL products under mild drought scenarios on an 11-year scale. Among them, significant increasing trends are observed in the southern part of the Songliao River Basin and the Huaihe River Basin, whereas significant decreasing trends are observed in the Pearl River Basin and the eastern part of the Yangtze River Basin, with the majority of pixels showing a decrease in the trigger threshold (69.6% for GSFC and 70.5% for JPL). This suggests that drought resistance to meteorological stress is decreasing. These results are consistent with those of the CSR. Additionally, despite accounting for the differences in spatial resolutions between the products, the percentage changes at different intervals compared to Fig. 8a also indicate the reliability of the dynamic threshold results from the CSR. Overall, the high degree of consistency between the static and dynamic perspectives of the GSFC and JPL results with the CSR not only confirms the reliability of the findings in this study, but also demonstrates the applicability of the proposed probability framework.

Fig. 10 Threshold changes in the GSFC and JPL products for triggering mild drought, and their absolute differences from CSR products. Histograms in panels show statistical proportions.

Fig. 11 Trends in thresholds for triggering mild drought for GSFC and JPL products under an 11-year sliding window.

5.2 Merits and limitations of the probability framework

We further performed a detailed analyses of the changes in the conditional probability of occurrence of mild, moderate, severe and extreme hydrological droughts under different meteorological stress conditions, based on the pixels in Fig. 2. Under the same CPA conditions, the conditional probabilities decreased sequentially as the drought class increased. The conditional probability increased significantly with increasing CPA stress (decreasing percentile), especially for the mild hydrological drought class, which eventually converged to almost 1 (Fig. 12). Moreover, the variation in the curves of different levels of drought between each pixel not only reflects differences in the resistance of terrestrial water storage system to precipitation deficit, but also proves the reliability of the probabilistic framework. Theoretically, precipitation deficit is a factor that directly leads to drought. The choice of 0.5 as the conditional probability was based on the consideration of the weak sensitivity of TWS to precipitation due to climate change and underlying surface factors, as shown in Fig. 4a for the northern and northwestern regions of China. The intensification of human activities such as groundwater overexploitation (Asoka et al., 2017), interregional water transfer (Long et al., 2020) and greenhouse gas emissions (Yuan et al., 2019) has significantly affected the regional water balance. It should be noted that the limited period for which GRACE data are available may restrict the number of actual hydrological drought events characterized. Consequently, the probability assessment may be overestimated. However, the given conditional probability in the framework is variable, and it depends mainly on the interdependence between the input variables. This flexibility in probability estimation enables the framework to be readily adapted to diverse regions, thus broadening its applicability.

However, this study has certain limitations. Firstly, we chose the Clayton copula model to describe the dependence structure between the CPA and TWSA-DSI, and the inherent uncertainty of this model propagates and affects the risk estimation of drought triggered under precipitation deficits (Leng and Hall, 2019). Secondly, the framework proposed in this study considers the CPA as the only conditional variable, without taking into account other factors that may influence drought, such as temperature, evaporation, and human activities. Despite the ability of copula functions to model the dependence between variables in three or even higher dimensions (e.g., vine copula), bivariate copula functions still have several advantages over trivariate copula functions in terms of computational efficiency, parameter estimation, and visualization (Nelsen, 2007; Cherubini et al., 2011). The choice of copula function should be based on a comprehensive consideration of the specific problem and characteristics of the data. If the observed sequences for univariate and multivariate models are not long enough, they may not provide sufficient constraints on the model parameters, especially for high-dimensional models (Sadegh et al., 2017). This also explains why this study focused on the pixels that showed a significant positive correlation between CPA and TWSA-DSI.

In addition, we further explored the conditional probability changes in the five aforementioned copula functions to assess their sensitivity. For each drought level, the conditional probability changes in all copula functions exhibited similarities, increasing as the CPA stress intensified and eventually approaching 1 (Fig. 13). In contrast, as drought levels and CPA stress intensified, the conditional probability changes of the Clayton copula became more pronounced. In fact, the drought situations of interest in this study required copula models that are more sensitive to the lower tail than the upper tail. This further confirms the accuracy and necessity of selecting the Clayton copula model for the proposed probability framework.

In general, the drought conditions represented by the TWSA-DSI encompass the combined signals of climate change and human activities, which represents an advantage over traditional single-type droughts. In addition, precipitation, as an input to the water balance, is typically the most direct and critical factor influencing the TWS. In this study, the use of the CPA as the only conditional variable takes into account the close relationship between precipitation and drought conditions. Moreover, the probabilistic framework can directly provide estimates of the precipitation deficit that triggers different levels of drought, which can significantly reduce data costs and facilitate detailed assessment of different combinations between the variables. These findings and approaches provide valuable insights and new avenues for a comprehensive understanding of drought formation mechanisms.

Fig. 12 Varying conditional probability of different CPA levels triggering different droughts in the four pixels, with the black dashed line indicating the set conditional probability.

Fig. 13 The CPA based on different copula functions triggers changes in the conditional probability of different levels of drought, with the black dashed line indicating the set conditional probability.

----

6. Conclusion

Currently, few studies have focused on drought trigger thresholds, especially in the context of human and climate change exacerbating drought while increasing uncertainty in induced drought. A precipitation-driven drought trigger threshold framework is proposed herein, which considers the multiscale characteristics of CPA and uses TWSA-DSI to characterize the hydrological drought. This study first identified the response time of drought to precipitation at each pixel to determine the CPA for the optimal scale of input. A probabilistic framework was then constructed using a copula function and conditional probabilities with various combinations of scenarios to derive probability assessments for triggering different levels of drought at a given CPA level. Thus, the precipitation thresholds corresponding to the triggering of different levels of drought could also be inferred from the given conditional probabilities. Furthermore, the dynamics of the trigger thresholds over time and the main drivers of these differences were explored.

This study found that the response time of drought to precipitation in China demonstrated significant spatial heterogeneity, with the differences mainly determined by the components of the TWS. Overall, CPA is closely related to TWSA-DSI, with weak or negative relationships in some places driven mostly by climate change and human activities. High-risk zones are identified based on the probability of a drought outbreak, and these locations typically have low trigger thresholds that dynamically decline over time, exacerbating the risk of drought. Moreover, changes in the water cycle due to climate change indirectly affect the dynamics of the thresholds. The method proposed in this study is helpful for understanding precipitation conditions to predict drought, and provides insight for better drought monitoring and management.

The framework is universal and can be applied to different regions. However, a limitation of this framework is that it requires identification or preprocessing of the connections between input variables in a given region/basin before it can be applied, and these are neither difficult nor unusual.

Acknowledgements

This research was jointly funded by the China Postdoctoral Science Foundation (grant no. 2022M722607), the National Natural Science Foundation of China (grant no. 52009102) and Young Talent fund of University Association for Science and Technology in Shaanxi, China (grant no. 20220710). We would like to express our sincere gratitude to the three anonymous reviewers for their insightful comments and constructive criticism, which helped us to improve this paper.

References

Allen, D. M., Mackie, D. C., Wei, M., 2004. Groundwater and climate change: a sensitivity analysis for the Grand Forks aquifer, southern British Columbia, Canada, 12(3), 270–290.

Azmi, M., Rüdiger, C., Walker, J. P., 2016. A data fusion - based drought index. Water Resources Research, 52(3), 2222-2239.

Asoka, A., Gleeson, T., Wada, Y., 2017. Relative contribution of monsoon precipitation and pumping to changes in groundwater storage in India. Nature Geoscience, 10(2), 109-117.

Alizadeh, M. R., Adamowski, J., Nikoo, M. R., 2020. A century of observations reveals increasing likelihood of continental-scale compound dry-hot extremes. Science advances, 6(39), eaaz4571.

Beguería, S., Vicente- Serrano, S. M., Reig, F., 2014. Standardized precipitation evapotranspiration index (SPEI) revisited: parameter fitting, evapotranspiration models, tools, datasets and drought monitoring. International journal of climatology, 34(10), 3001-3023.

Cherubini, U., Mulinacci, S., Gobbi, F., 2011. Dynamic copula methods in finance. John Wiley & Sons.

Chen, H., Sun, J., 2015. Changes in drought characteristics over China using the standardized precipitation evapotranspiration index. Journal of Climate, 28(13), 5430-5447.

Coelho, C. A., Cardoso, D. H., Firpo, M. A., 2016. Precipitation diagnostics of an exceptionally dry event in São Paulo, Brazil. Theoretical and applied climatology, 125, 769-784.

Chiang, F., Mazdiyasni, O., AghaKouchak, A., 2018. Amplified warming of droughts in southern United States in observations and model simulations. Science Advances, 4(8), eaat2380.

Cai, Y., Guan, K., Lobell, D., 2019. Integrating satellite and climate data to predict wheat yield in Australia using 870 machine learning approaches. Agric. For. Meteorol. 274, 144–159.

Chen, H., Wang, S., Zhu, J., 2020. Projected changes in abrupt shifts between dry and wet extremes over China through an ensemble of regional climate model simulations. Journal of Geophysical Research: Atmospheres, 125(23), e2020JD033894.

Condon, L. E., Atchley, A. L., Maxwell, R.M., 2020. Evapotranspiration depletes groundwater under warming over the contiguous united states. Nat. Commun. 11 (1), 873.

Chen, J., Tapley, B., Tamisiea, M. E., 2021. Error Assessment of GRACE and GRACE Follow-On Mass Change. Journal of Geophysical Research: Solid Earth, 126(9), e2021JB022124.

Cui, A., Li, J., Zhou, Q., 2021. Use of a multiscalar GRACE-based standardized terrestrial water storage index for assessing global hydrological droughts. Journal of Hydrology, 603, 126871.

Chen, J., Gao, M., Cheng, S., 2022. Global 1 km× 1 km gridded revised real gross domestic product and electricity consumption during 1992–2019 based on calibrated nighttime light data. Scientific Data, 9(1), 202.

Fensholt, R., Langanke, T., Rasmussen, K., 2012. Greenness in semi-arid areas across the globe 1981–2007—an Earth Observing Satellite based analysis of trends and drivers. Remote sensing of environment, 121, 144-158.

Field, C. B., Barros, V., Stocker, T. F., 2012. Managing the risks of extreme events and disasters to advance climate change adaptation: special report of the intergovernmental panel on climate change. Cambridge University Press.

Famiglietti J S, Rodell M. Water in the Balance. Science, 2013, 340(6138): 1300-1301.

Feng, X., Fu, B., Piao, S., 2016. Revegetation in China's Loess Plateau is approaching sustainable water resource limits. Nature Climate Change 6 (11), 1019–1022.

Fang, W., Huang, S., Huang, Q., 2019. Probabilistic assessment of remote sensing-based terrestrial vegetation vulnerability to drought stress of the Loess Plateau in China. Remote sensing of environment, 232, 111290.

Green, T.R., Taniguchi, M., Kooi, H., 2011. Beneath the surface of global change: impacts of climate change on groundwater. J. Hydrol. 405 (3–4), 532–560.

Gu, L., Chen, J., Yin, J., 2020. Responses of precipitation and runoff to climate warming and implications for future drought changes in China. Earth's Future, 8(10), e2020EF001718.

Guo, Y., Huang, Q., Huang, S., 2021. Elucidating the effects of mega reservoir on watershed drought tolerance based on a drought propagation analytical method. Journal of Hydrology, 598, 125738.

Guo, W., Huang, S., Huang, Q., 2023. Drought trigger thresholds for different levels of vegetation loss in China and their dynamics. Agricultural and Forest Meteorology, 331, 109349.

Hao, Z., Singh, V.P., 2015. Drought characterization from a multivariate perspective: A review. Journal of Hydrology. 527, 668–678.

Hong, X., Guo, S., Zhou, Y., 2015. Uncertainties in assessing hydrological drought using streamflow drought index for the upper Yangtze River basin. Stochastic Environmental Research and Risk Assessment, 29, 1235-1247.

Hong, Y., Nix, H. A., Hutchinson, M. F., 2005. Spatial interpolation of monthly mean climate data for China. International Journal of Climatology: A Journal of the Royal Meteorological Society, 25(10), 1369-1379.

Herrera-Estrada, J.E., Satoh, Y., Sheffield, J., 2017. Spatiotemporal dynamics of global drought. Geophysical Research Letters, 44(5): 2254-2263.

Huang, T., Xu, L., Fan, H., 2018. Temporal and spatial variation characteristics and the evolution trends of droughts in the Yangtze River Basin. Research of Environmental Sciences, 31(10):1677-1684. (in Chinese)

Han, Z., Huang, S., Huang, Q., 2021a. GRACE-based high-resolution propagation threshold from meteorological to groundwater drought. Agricultural and Forest Meteorology, 307, 108476.

Han, Z., Huang, Q., Huang, S., 2021b. Spatial-temporal dynamics of agricultural drought in the Loess Plateau under a changing environment: Characteristics and potential influencing factors. Agricultural Water Management, 244, 106540.

Jin, Z., Guo, L., Lin, H., 2018. Soil moisture response to rainfall on the Chinese Loess Plateau after a long-term vegetation rehabilitation. Hydrol. Process. 32 (12), 1738–1754.

Jin, H., Chen, X., Wu, P., 2021. Evaluation of spatial-temporal distribution of precipitation in mainland China by statistic and clustering methods. Atmospheric Research, 262, 105772.

Jiang, W., Niu, Z., Wang, L., 2022. Impacts of Drought and Climatic Factors on Vegetation Dynamics in the Yellow River Basin and Yangtze River Basin, China. Remote Sensing, 14(4), 930.

King, A. D., Pitman, A. J., Henley, B. J., 2020. The role of climate variability in Australian drought. Nature Climate Change, 10(3), 177-179.

Li, W., Yi, X., Hou, M., 2012. Standardized precipitation evapotranspiration index shows drought trends in China. Chinese Journal of Eco-Agriculture, 20(5): 643–649. (in Chinese)

Lloyd-Hughes, B.,2014. The impracticality of a universal drought definition. Theoretical and Applied Climatology, 117(3–4), 607–611

Long, D., Shen, Y.J., Sun, A.Y., 2014. Drought and flood monitoring for a large karst plateau in Southwest China using extended GRACE data. Remote Sensing of Environment, 145–160.

Long, D., Pan, Y., Zhou, J., 2017. Global analysis of spatiotemporal variability in merged total water storage changes using multiple GRACE products and global hydrological models. Remote sensing of environment, 192, 198-216.

Li, Y., Piao, S., Li, L. Z., 2018. Divergent hydrological response to large-scale afforestation and vegetation greening in China. Science Advances, 4(5), eaar4182.

Leng, G., Hall, J., 2019. Crop yield sensitivity of global major agricultural countries to droughts and the projected changes in the future. Science of the Total Environment, 654, 811-821.

Li, X., Li, Y., Chen, A., 2019. The impact of the 2009/2010 drought on vegetation growth and terrestrial carbon balance in Southwest China. Agricultural and Forest Meteorology, 269, 239-248.

Long, D., Yang, W.T., Scanlon, B.R., 2020. South-to-North Water Diversion stabilizing Beijing’s groundwater levels. Nature communications, 11 (2020), 1863–1880, 2020.

Li, F., Kusche, J., Chao, N., 2021. Long-term (1979-present) total water storage anomalies over the global land derived by reconstructing GRACE data. Geophysical Research Letters, 48, e2021GL093492.

Liu, Q., Yang, Y., Liang, L., 2023. Thresholds for triggering the propagation of meteorological drought to hydrological drought in water-limited regions of China. Science of The Total Environment, 876, 162771.

Ma, Z., Fu, Z., Yang, Q., 2018. Drying trend in Northern China and its shift during 1951-2016. Chinese Journal of Atmospheric Sciences, 42(4): 951-961. (in Chinese)

Miao, C., Gou, J., Fu, B., 2022. High-quality reconstruction of China’s natural streamflow. Science Bulletin, 67(5), 547-556.

Nelsen, R. B., 2007. An Introduction to Copulas Springer Science & Business Media.

Peter D, H., 1985. Kernel estimation of a distribution function. Communications in Statistics-Theory and Methods, 14(3), 605-620.

Prugh, L. R., Deguines, N., Grinath, J. B., 2018. Ecological winners and losers of extreme drought in California. Nature Climate Change, 8(9), 819-824.

Pokhrel, Y., Felfelani, F., Satoh, Y., 2021. Global terrestrial water storage and drought severity under climate change. Nature Climate Chang. 11, 226–233.

Quinlan, J. R., 1986. Induction of decision trees. Machine learning. 81-106.

Stine, R. A., 1995. Graphical interpretation of variance inflation factors. The American Statistician, 49, 53–56.

Svoboda, M., LeComte, D., Hayes, M., 2002. The drought monitor. Bulletin of the American Meteorological Society, 83(8), 1181-1190.

Sun, C., Yang, S., 2012. Persistent severe drought in southern China during winter–spring 2011: Large‐scale circulation patterns and possible impacting factors. Journal of Geophysical Research: Atmospheres, 117(D10).

Santhosh, D., Srinivas, V. V., 2013. Bivariate frequency analysis of floods using a diffusion based kernel density estimator. Water Resources Research, 49(12), 8328-8343.

Santos, J. F., Portela, M. M., Naghettini, M., 2013. Precipitation thresholds for drought recognition: a further use of the standardized precipitation index, SPI. WIT Transactions on Ecology and the Environment, 172, 3-14.

Sinha, D., Syed, T.H., Famiglietti, J.S., 2017. Characterizing drought in India using GRACE observations of terrestrial water storage deficit. J. Hydrometeorol. 18 (2), 381–396.

Sadegh, M., Ragno, E., AghaKouchak, A., 2017. Multivariate Copula Analysis Toolbox (MvCAT): describing dependence and underlying uncertainty using a Bayesian framework. Water Resources Research, 53(6), 5166-5183.

Scanlon, B. R., Zhang, Z., Save, H., 2018. Global models underestimate large decadal declining and rising water storage trends relative to GRACE satellite data. Proceedings of the National Academy of Sciences, 115(6), E1080-E1089.

Sattar, M.N., Lee, J.Y., Shin, J.Y., 2019. Probabilistic characteristics of drought propagation from meteorological to hydrological drought in South Korea. Water Recourse Management. 33, 2439–2452.

Schumacher, D. L., Keune, J., Van Heerwaarden, C. C., 2019. Amplification of mega-heatwaves through heat torrents fuelled by upwind drought. Nature Geoscience, 12(9), 712-717.

Sun, A. Y., Scanlon, B. R., Zhang, Z., 2019. Combining physically based modeling and deep learning for fusing GRACE satellite data: can we learn from mismatch?. Water Resources Research, 55(2), 1179-1195.

Sinha, D., Syed, T. H., Reager, J. T., 2019. Utilizing combined deviations of precipitation and GRACE-based terrestrial water storage as a metric for drought characterization: A case study over major Indian river basins. Journal of Hydrology, 572: 294-307.

Sun, Z., Long, D., Yang, W., 2020. Reconstruction of GRACE data on changes in total water storage over the global land surface and 60 basins. Water Resources Research, 56(4), e2019WR026250.

Singh, A., Reager, J. T., Behrangi, A., 2021. Estimation of hydrological drought recovery based on precipitation and Gravity Recovery and Climate Experiment (GRACE) water storage deficit. Hydrology and Earth System Sciences, 25(2), 511-526.

Van den Broeke, M., Bamber, J., Ettema, J., 2009. Partitioning recent Greenland mass loss. science, 326(5955), 984-986.

Vicente-Serrano, S.M., Beguería, S., López-Moreno, J.I., 2010. A multi-scalar drought index sensitive to global warming: the Standardized Precipitation Evapotranspiration Index - SPEI. Journal of Climate, 23(7), 1696-1718.

Van Loon, A.F., Van Huijgevoort, M.H.J., Van Lanen, H.A.J., 2012. Evaluation of drought propagation in an ensemble mean of large-scale hydrological models. Hydrol. Earth Syst. Sci., 16:4057-4078.

Van Loon, A. F., Gleeson, T., Clark, J., 2016. Drought in the anthropocene. Nature Geoscience, 9, 89

Wang, J., Li, X., Christakos, G., 2010. Geographical detectors-based health risk assessment and its application in the neural tube defects study of the Heshun Region, China. International Journal of Geographical Information Science, 24(1), 107-127.

Wang, L., Huang, S., Huang, Q., 2021. Vegetation vulnerability and resistance to hydrometeorological stresses in water-and energy-limited watersheds based on a Bayesian framework. Catena, 196, 104879.

Wu, J., Chen, X., Yao, H., 2021. Multi-timescale assessment of propagation thresholds from meteorological to hydrological drought. Science of the Total Environment, 765, 144232.

Yang, Z., Li, W., Yan, Z., 2019. The relationship between temperature change and electrical power demand-evidence from China's Urban Panel Data from 2000 to 2014. Journal of Beijing Institute of Technology (Social Sciences Edition), 21(05):44-55. (in Chinese)

Yuan, X., Wang, L., Wu, P., 2019. Anthropogenic shift towards higher risk of flash drought over China. Nature communications, 10(1), 1-8.

Yu, R., Zhai, P., 2020. More frequent and widespread persistent compound drought and heat event observed in China. Scientific Reports, 10(1), 1-7.

Zhang, Q., Han, L., Zhang, Li., 2014. Analysis on the character and management strategy of drought disaster and risk under the climate warming. Advances in Earth Science, 29(1): 80-91. (in Chinese)

Zhao, M., Geruo, A., Velicogna, I., 2017. A global gridded dataset of GRACE drought severity index for 2002–14: Comparison with PDSI and SPEI and a case study of the Australia millennium drought. Journal of Hydrometeorology, 18(8), 2117-2129.

Zhong, Y., Feng W., Zhong M, 2020. Dataset of reconstructed terrestrial water storage in China based on precipitation (2002-2019). National Tibetan Plateau Data Center.

Zhao, M., Geruo, A., Zhang, J., 2021. Ecological restoration impact on total terrestrial water storage. Nature Sustainability, 4(1), 56-62.

List of Figure Captions

Fig. 5 Probability of triggering different levels (mild, moderate, severe and extreme) of drought under different percentile precipitation scenarios. The different CPA and TWSA-DSI scenarios are represented by the X and Y in the panel.

Fig. 6 CPA corresponding to different levels of drought trigger thresholds. The white pixels in the panel indicate no threshold, and the same applies to subsequent figures.

Fig. 7 CPA percentiles corresponding to different levels of drought trigger thresholds.

Fig. 8 Spatial trends in thresholds corresponding to mild drought under sliding windows of 11 (a), 9 (b), and 7 years (c), with black markers indicating significance at the 0.05 level. Histograms in panels show statistical proportions.

Fig. 9 Relative importance of various factors on triggering thresholds under sliding windows of 11 (a), 9 (b), and 7 years (c). Note: PGI, VPD, T, ES, NDVI, r and NSE represent population-GDP index, vapor pressure deficit, air temperature, evaporation flux from soil, normalized vegetation index, correlation coefficient and Nash-Sutcliffe efficiency respectively.

Fig. 10 Threshold changes in the GSFC and JPL products for triggering mild drought, and their absolute differences from CSR products. Histograms in panels show statistical proportions.

Fig. 11 Trends in thresholds for triggering mild drought for GSFC and JPL products under an 11-year sliding window.

Fig. 12 Varying conditional probability of different CPA levels triggering different droughts in the four pixels, with the black dashed line indicating the set conditional probability.

Fig. 13 The CPA based on different copula functions triggers changes in the conditional probability of different levels of drought, with the black dashed line indicating the set conditional probability.

Fig. S1 Boxplot of the VIF variation between factors on sliding scale over 11 (a), 9 (b) and 7 years (c).

Fig. S2 Correlation of TWSA-DSI with CPA based on GSFZ and JPL products and their response time variation.

Fig. S3 Changes in CPA corresponding to triggered mild and extreme drought based on GSFZ and JPL products, respectively. White pixels in the panel indicate no threshold.

Figure 1

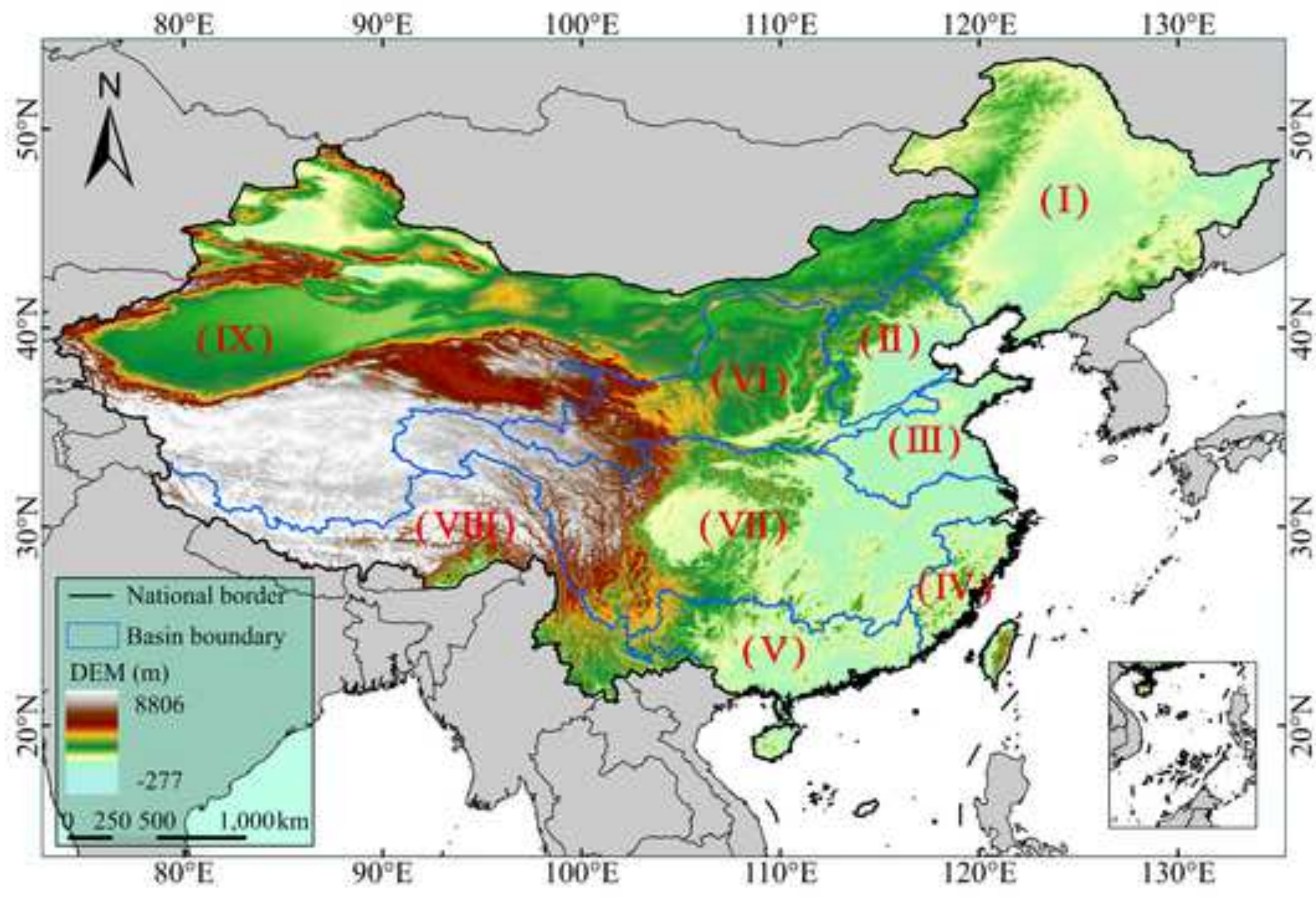
80°E
90°E
100°E
110°E
120°E
130°E
50°N
40°N
30°N
20°N
N
(I)
(II)
(III)
(IV)
(V)
(VI)
(VII)
(VIII)
(IX)
National border
Basin boundary
DEM (m)
8806
-277
0 250 500 1,000km

Figure 2

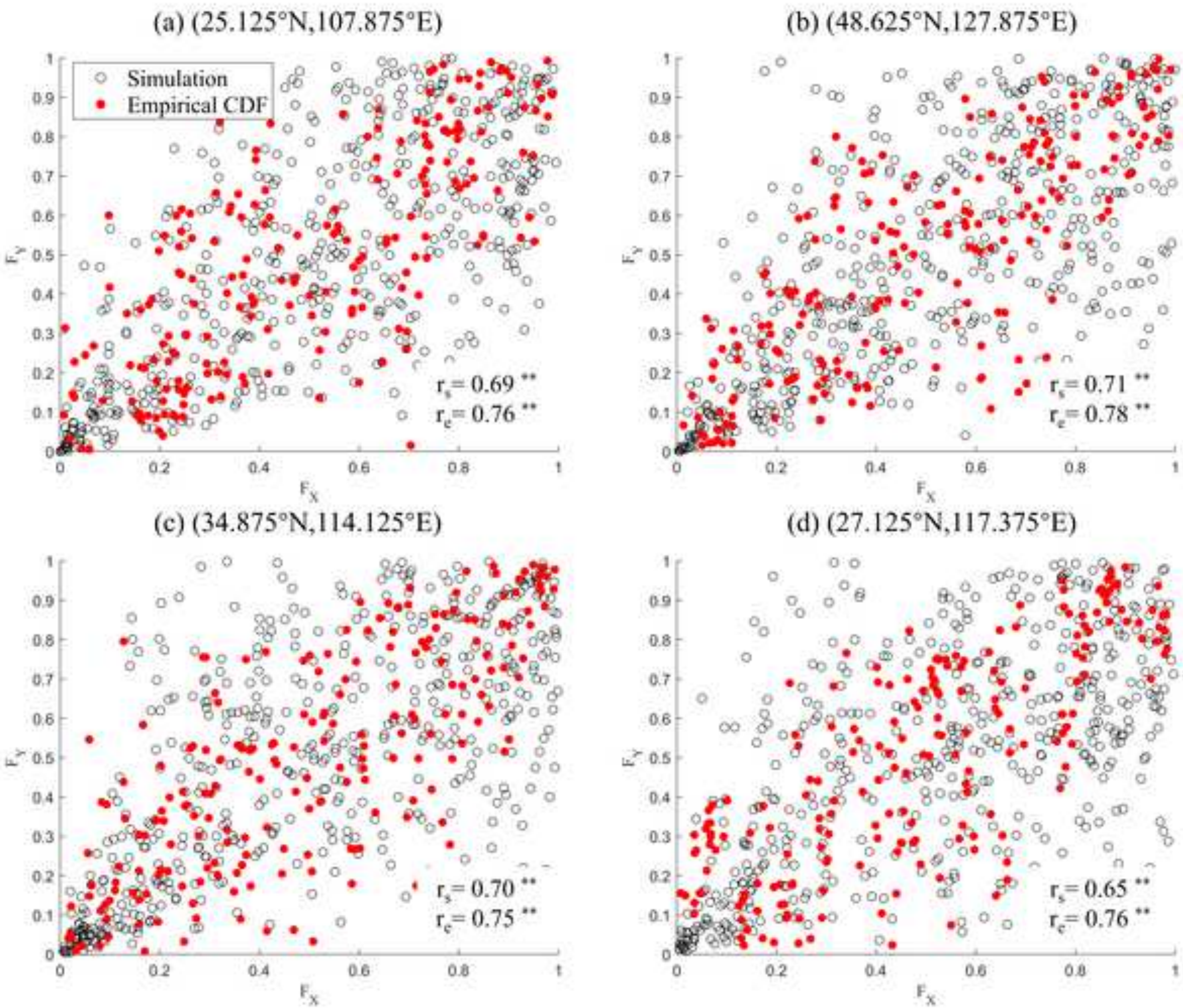

(a) (25.125°N,107.875°E)
(b) (48.625°N,127.875°E)
(c) (34.875°N,114.125°E)
(d) (27.125°N,117.375°E)
Simulation
Empirical CDF
r_s= 0.69 **
r_e= 0.76 **
r_s= 0.71 **
r_e= 0.78 **
r_s= 0.70 **
r_e= 0.75 **
r_s= 0.65 **
r_e= 0.76 **
F_X
F_Y
0
0.1
0.2
0.3
0.4
0.5
0.6
0.7
0.8
0.9
1

Figure 3

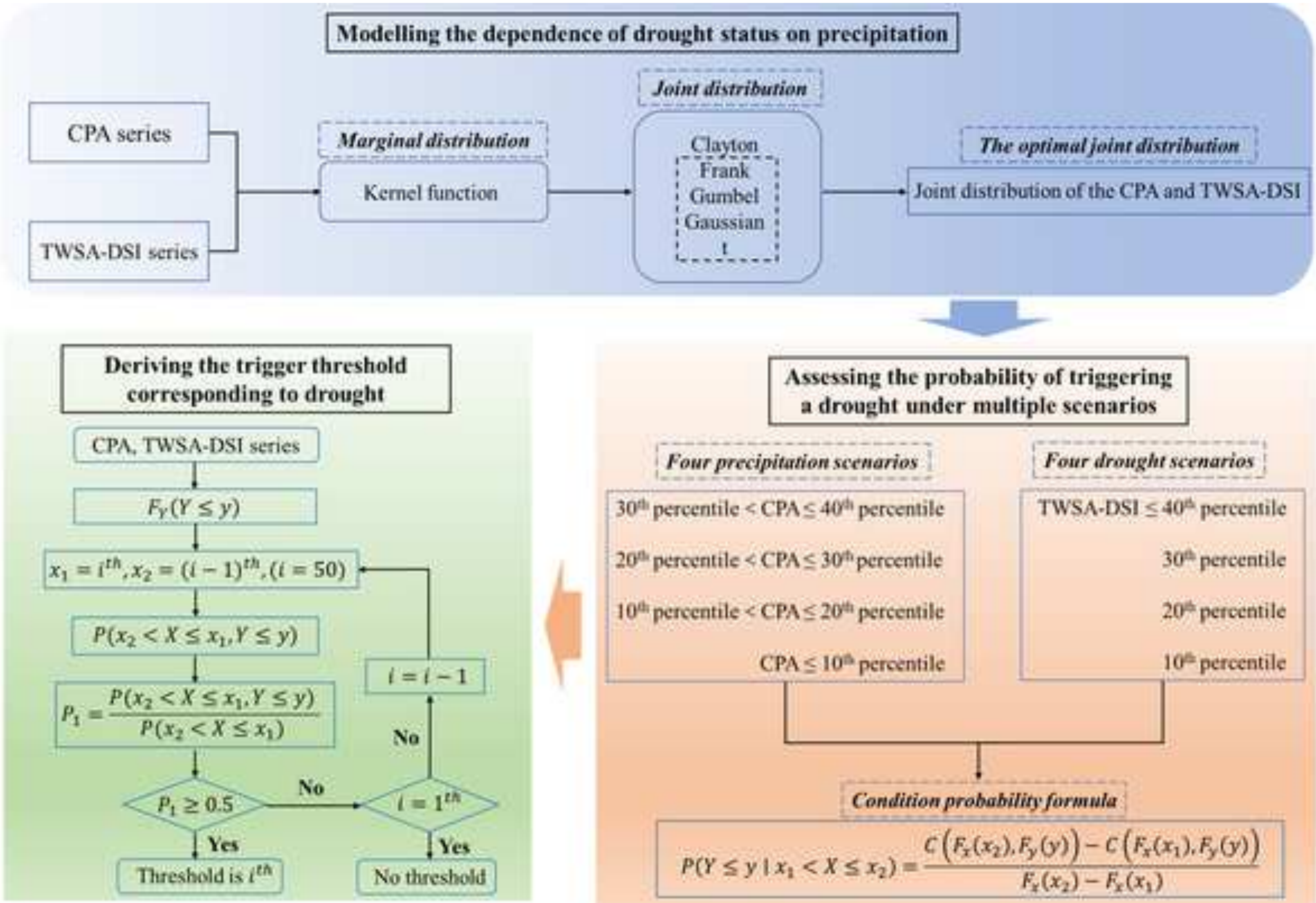

Modelling the dependence of drought status on precipitation
CPA series
TWSA-DSI series
Marginal distribution
Kernel function
Joint distribution
Clayton
Frank
Gumbel
Gaussian
t
The optimal joint distribution
Joint distribution of the CPA and TWSA-DSI
Deriving the trigger threshold corresponding to drought
CPA, TWSA-DSI series
$F_Y(Y \leq y)$
$x_1 = i^{th}, x_2 = (i-1)^{th}, (i = 50)$
$P(x_2 < X \leq x_1, Y \leq y)$
$P_1 = \frac{P(x_2 < X \leq x_1, Y \leq y)}{P(x_2 < X \leq x_1)}$
$P_1 \geq 0.5$
No
$i = 1^{th}$
No
$i = i - 1$
Yes
Threshold is i^{th}
Yes
No threshold
Assessing the probability of triggering a drought under multiple scenarios
Four precipitation scenarios
30th percentile < CPA ≤ 40th percentile
20th percentile < CPA ≤ 30th percentile
10th percentile < CPA ≤ 20th percentile
CPA ≤ 10th percentile
Four drought scenarios
TWSA-DSI ≤ 40th percentile
30th percentile
20th percentile
10th percentile
Condition probability formula
$P(Y \leq y \mid x_1 < X \leq x_2) = \frac{C(F_x(x_2), F_y(y)) - C(F_x(x_1), F_y(y))}{F_x(x_2) - F_x(x_1)}$

Figure 4

Click here to access/download;Figure;Figure 4.tif

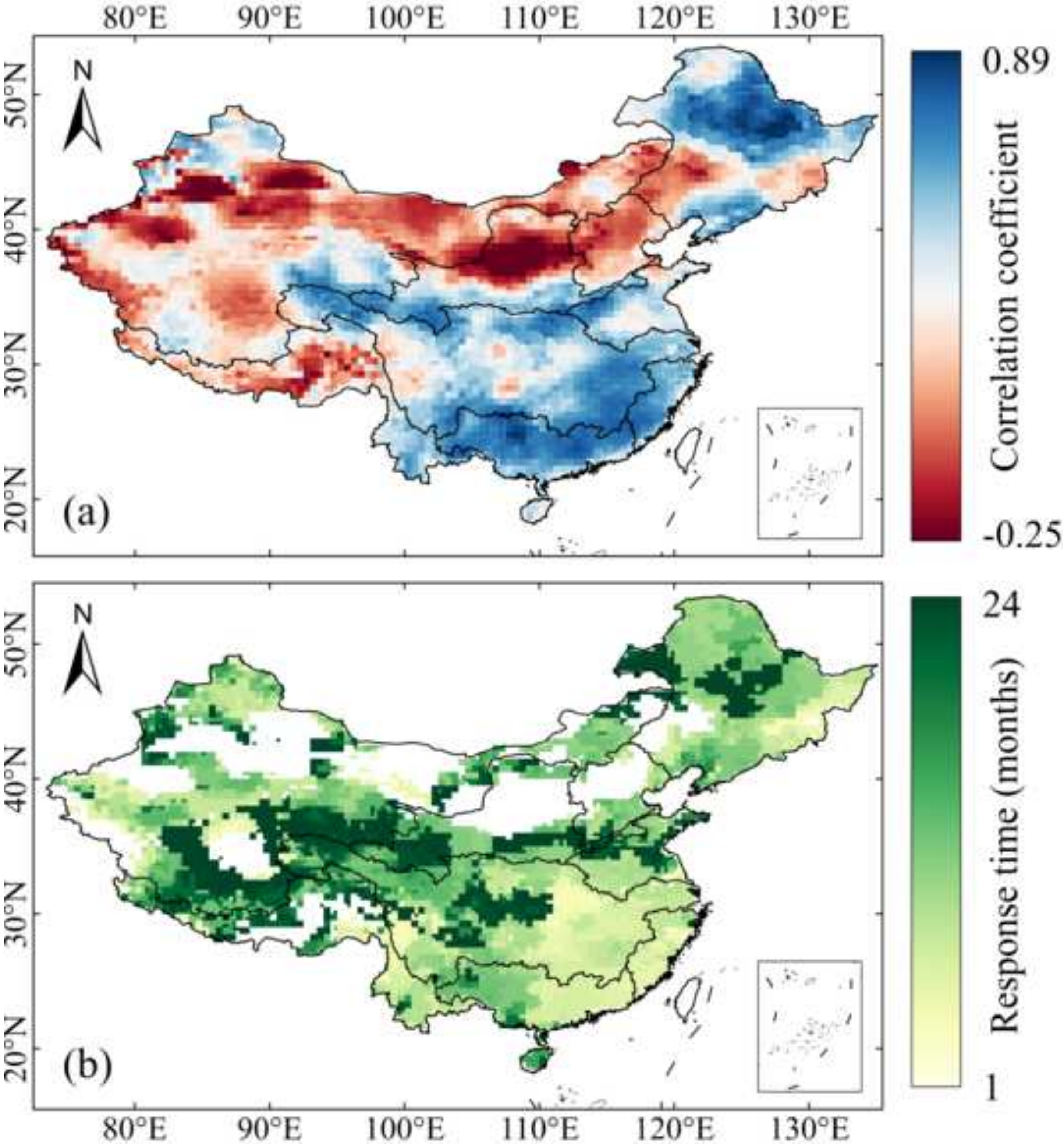

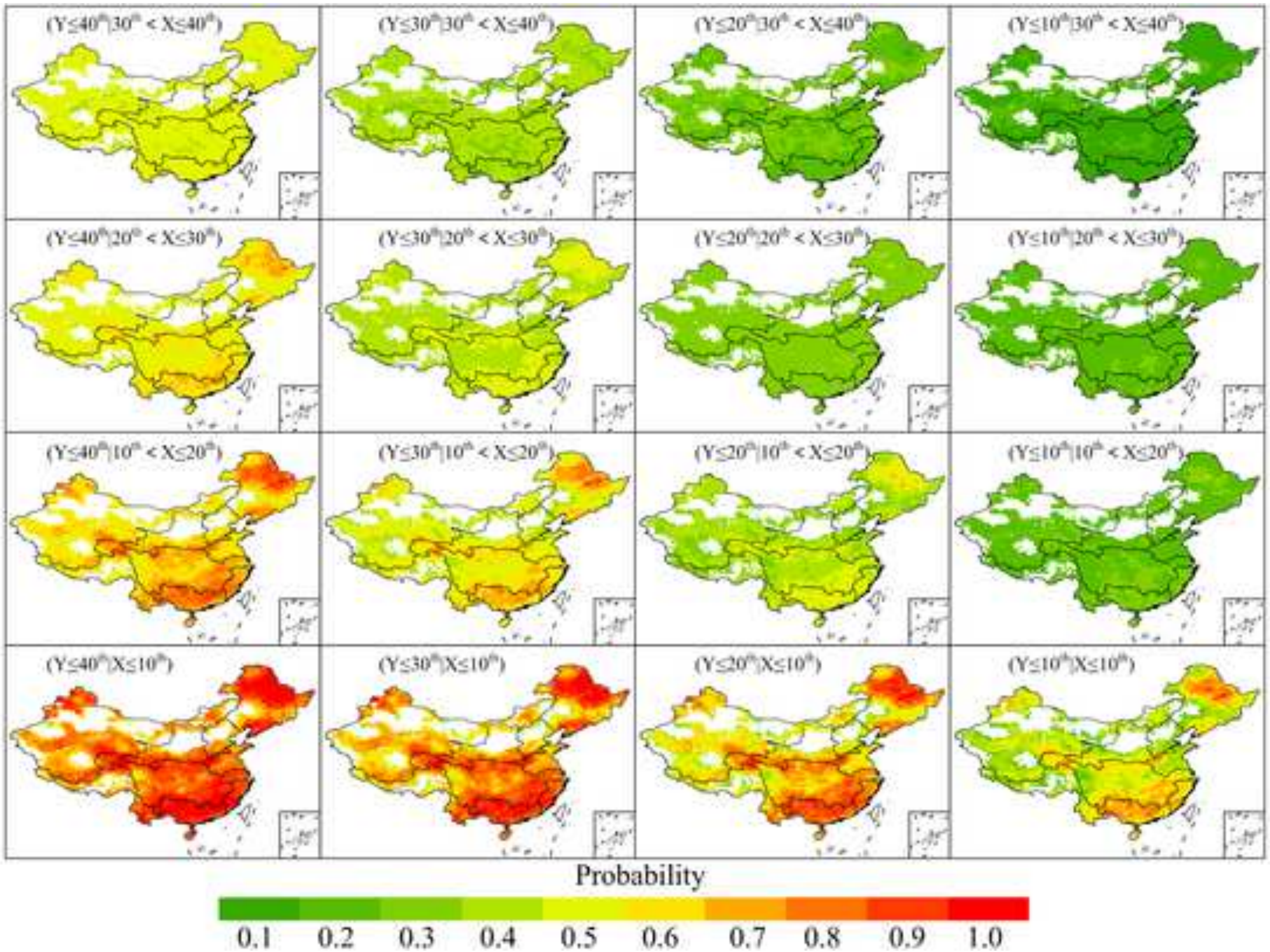
(Y≤40th|30th < X≤40th)
(Y≤30th|30th < X≤40th)
(Y≤20th|30th < X≤40th)
(Y≤10th|30th < X≤40th)
(Y≤40th|20th < X≤30th)
(Y≤30th|20th < X≤30th)
(Y≤20th|20th < X≤30th)
(Y≤10th|20th < X≤30th)
(Y≤40th|10th < X≤20th)
(Y≤30th|10th < X≤20th)
(Y≤20th|10th < X≤20th)
(Y≤10th|10th < X≤20th)
(Y≤40th|X≤10th)
(Y≤30th|X≤10th)
(Y≤20th|X≤10th)
(Y≤10th|X≤10th)
Probability
0.1 0.2 0.3 0.4 0.5 0.6 0.7 0.8 0.9 1.0

Figure 6

Click here to access/download;Figure;Figure 6.tif

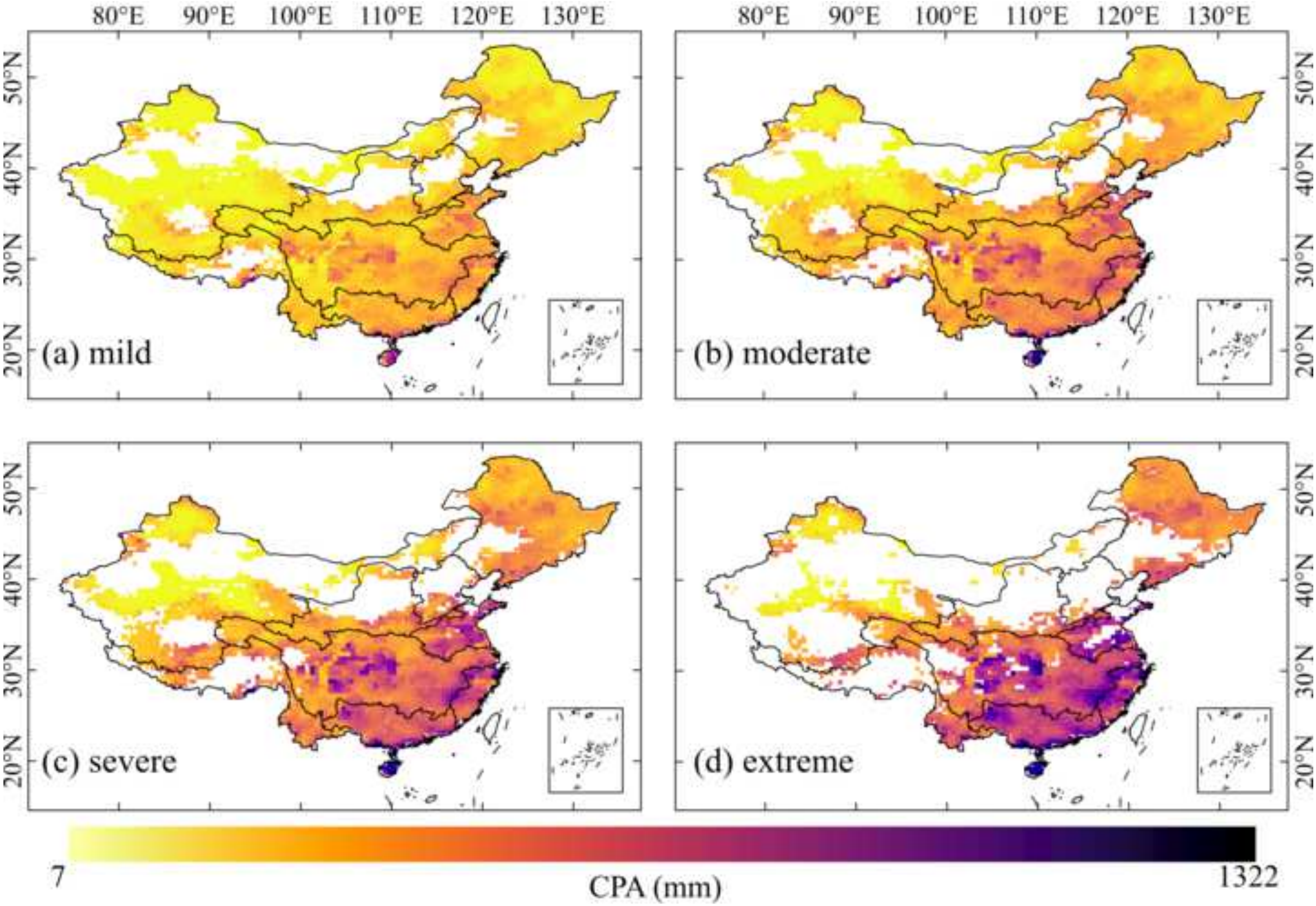

Figure 7

Click here to access/download;Figure;Figure 7.tif

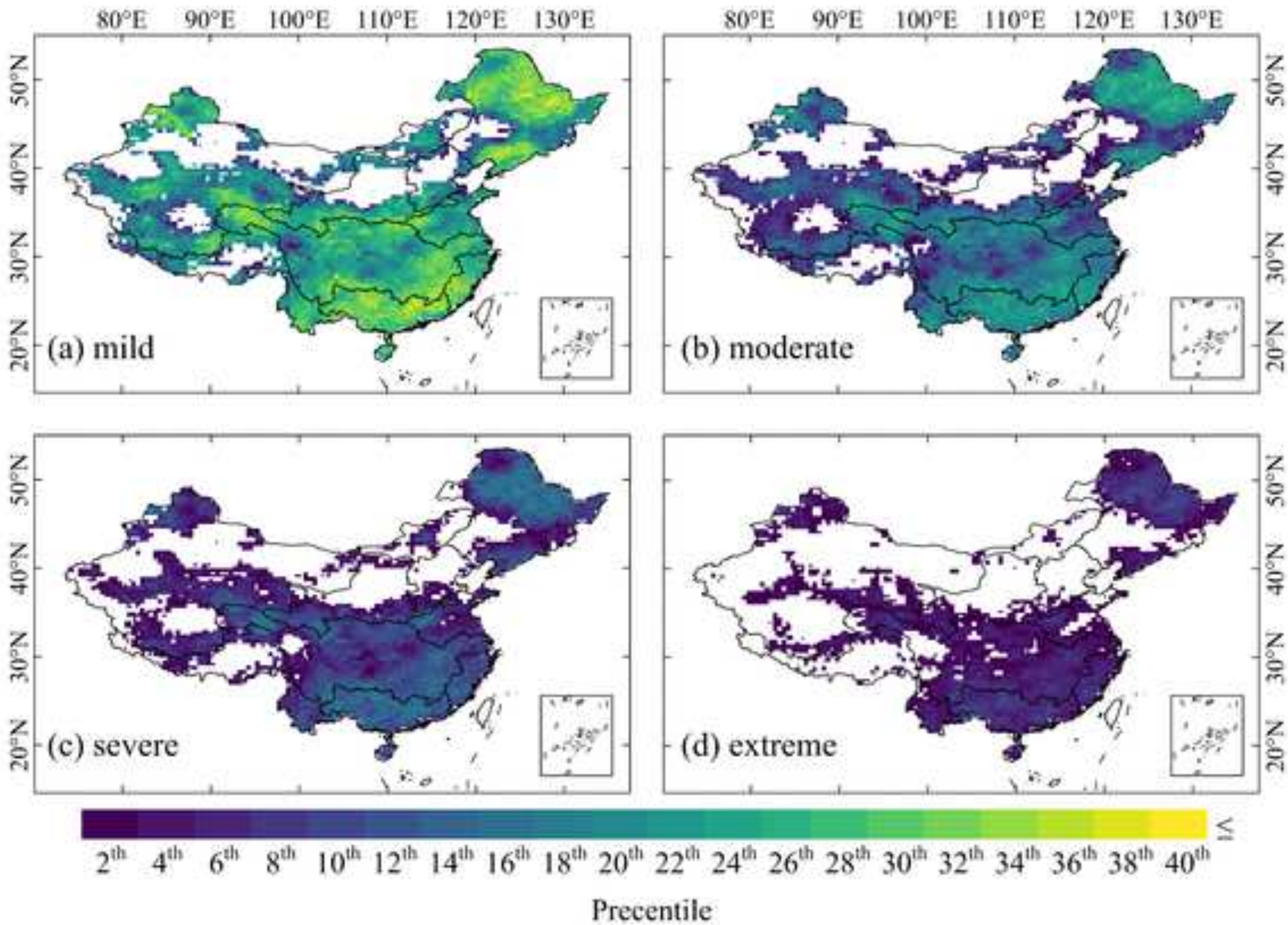

Figure 8

Click here to access/download;Figure;Figure 8.tif

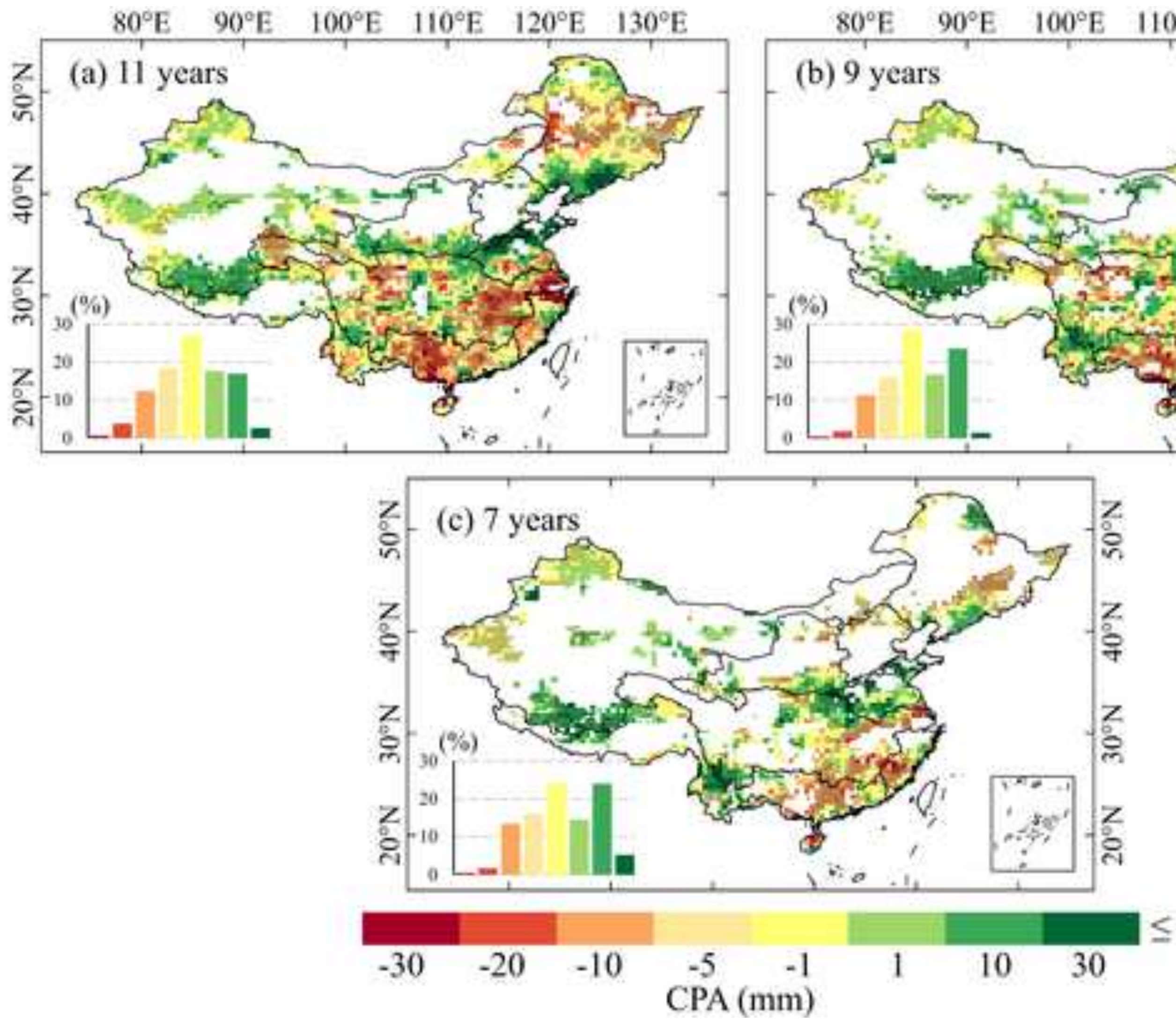

Figure 9

Click here to access/download;Figure;Figure 9.tif

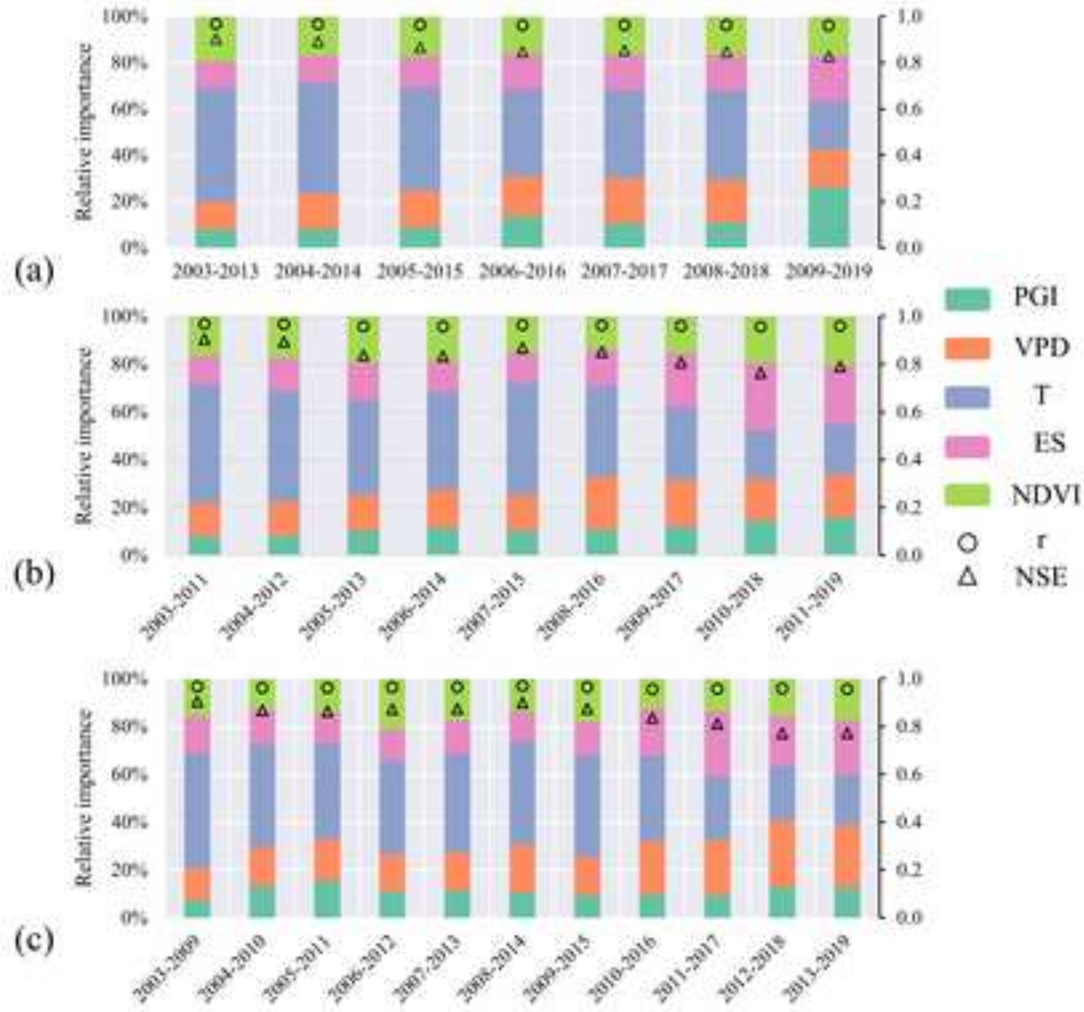

Figure 10

Click here to access/download;Figure;Figure 10.tif

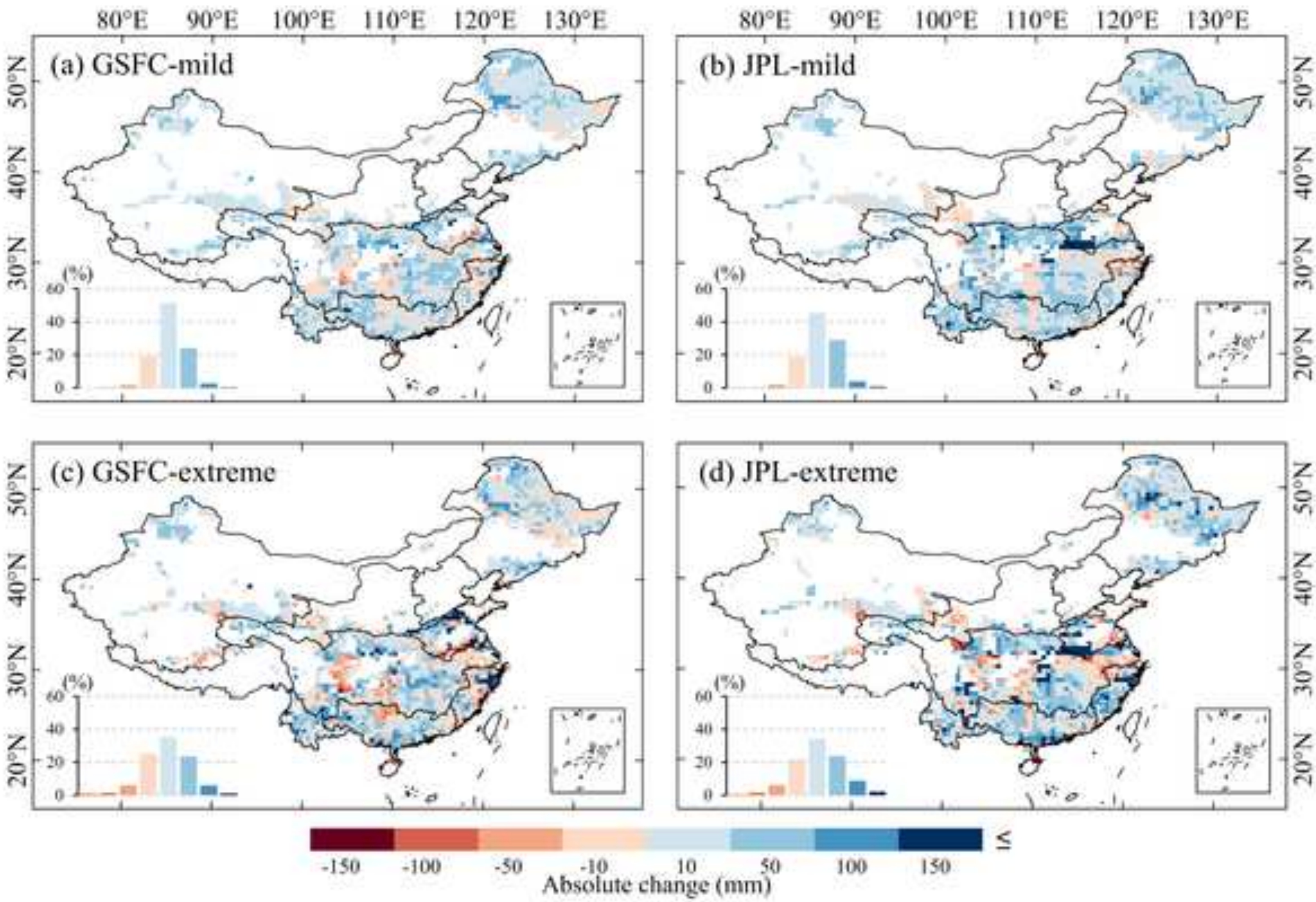

Figure 11

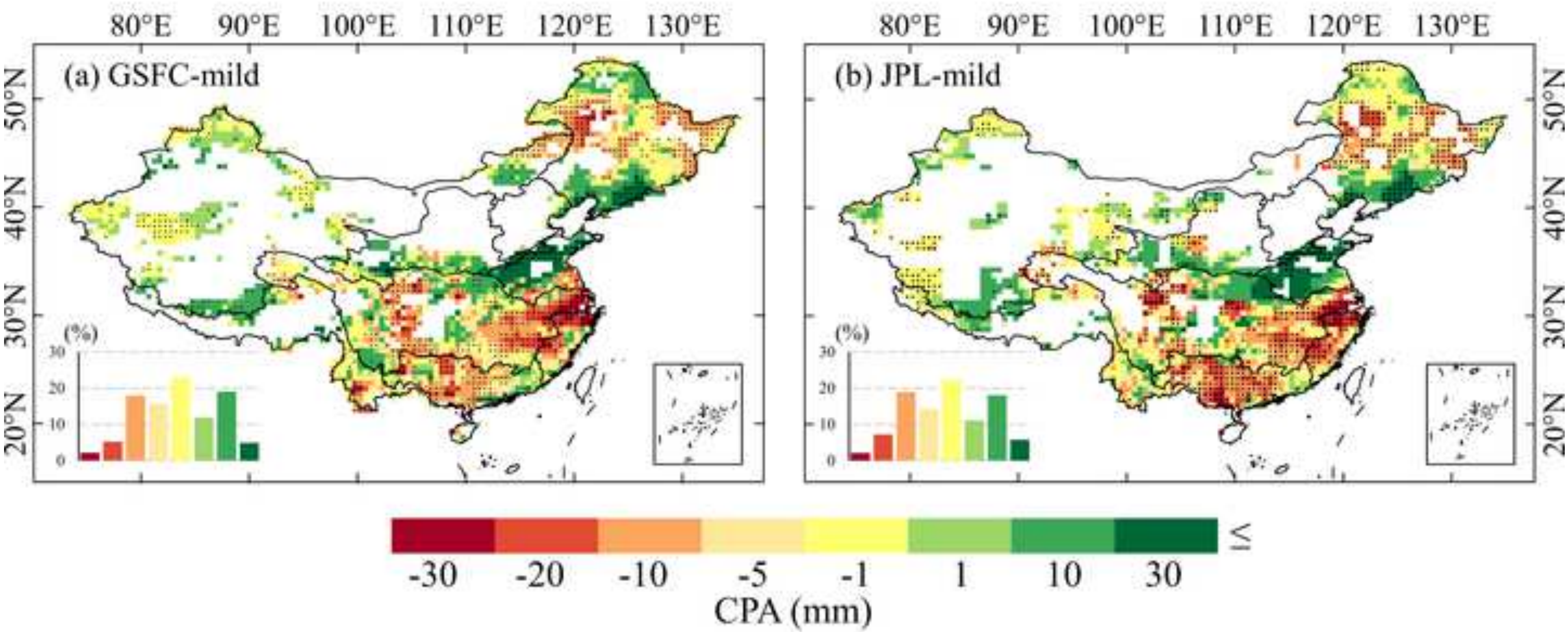
80°E
90°E
100°E
110°E
120°E
130°E
50°N
40°N
30°N
20°N
(a) GSFC-mild
(b) JPL-mild
(%)
30
20
10
0
-30
-20
-10
-5
-1
1
10
30
≤
CPA (mm)

Figure 12

Click here to access/download;Figure;Figure 12.tif

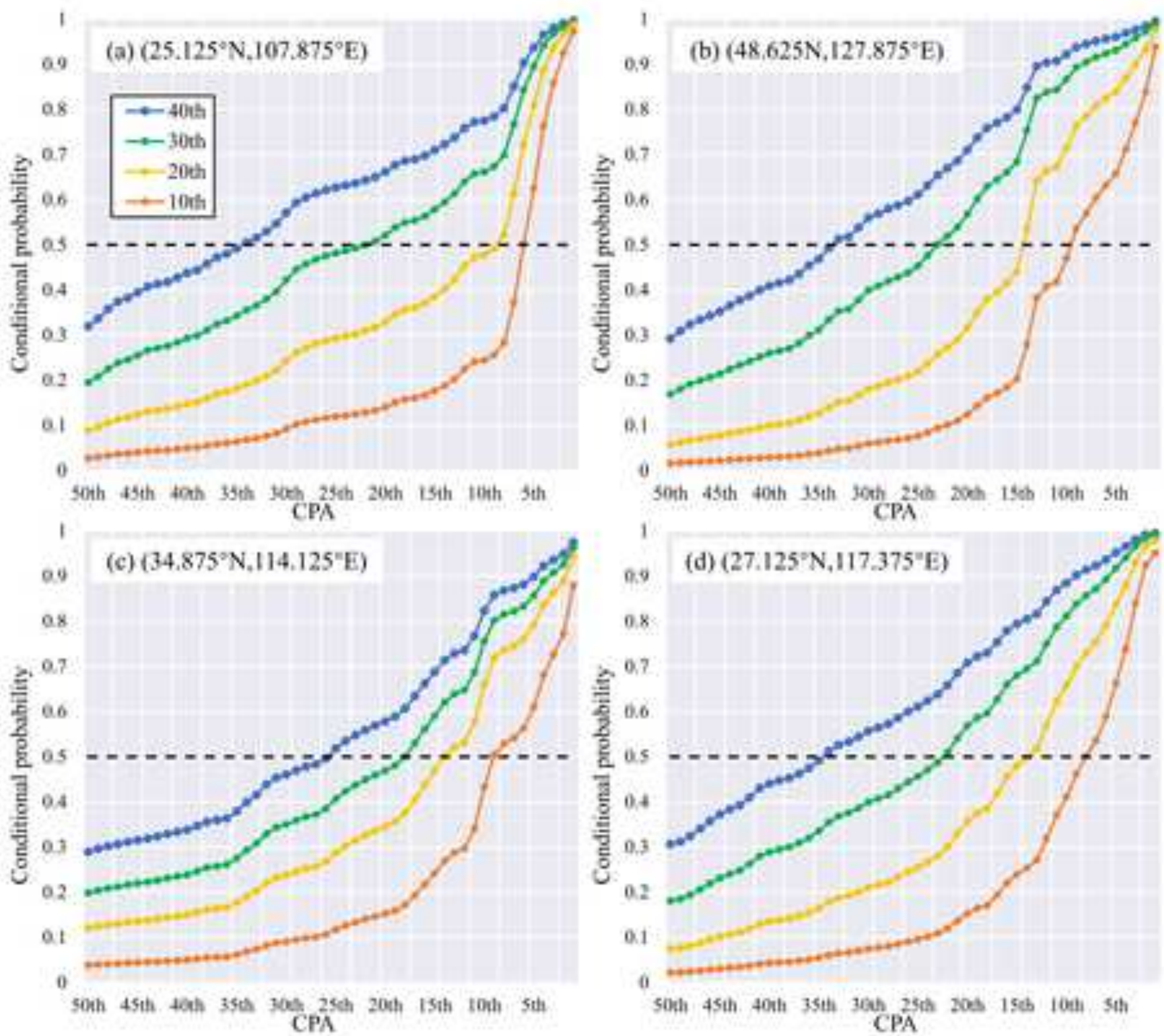

Figure 13

Click here to access/download;Figure;Figure 13.tif

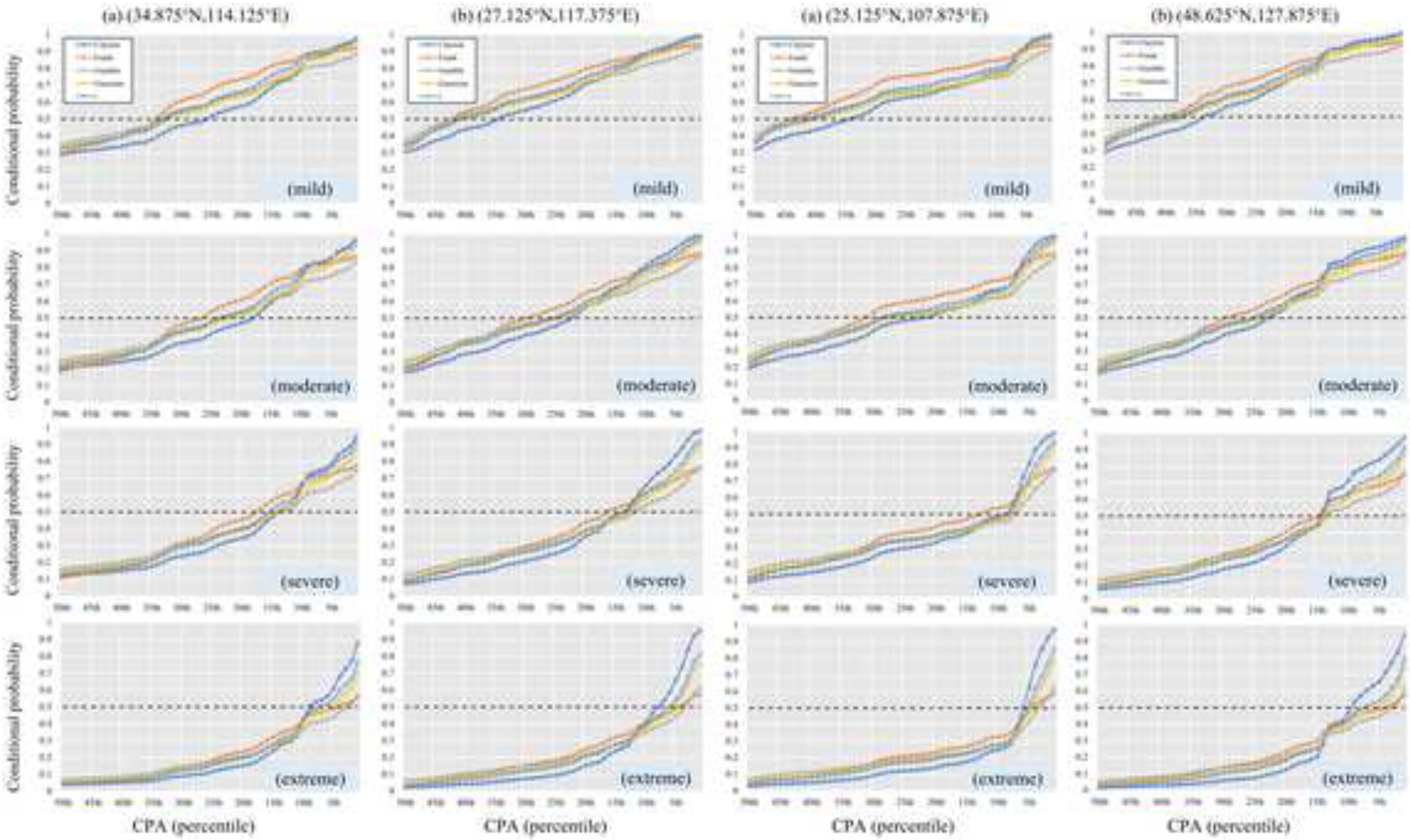

Figure S1

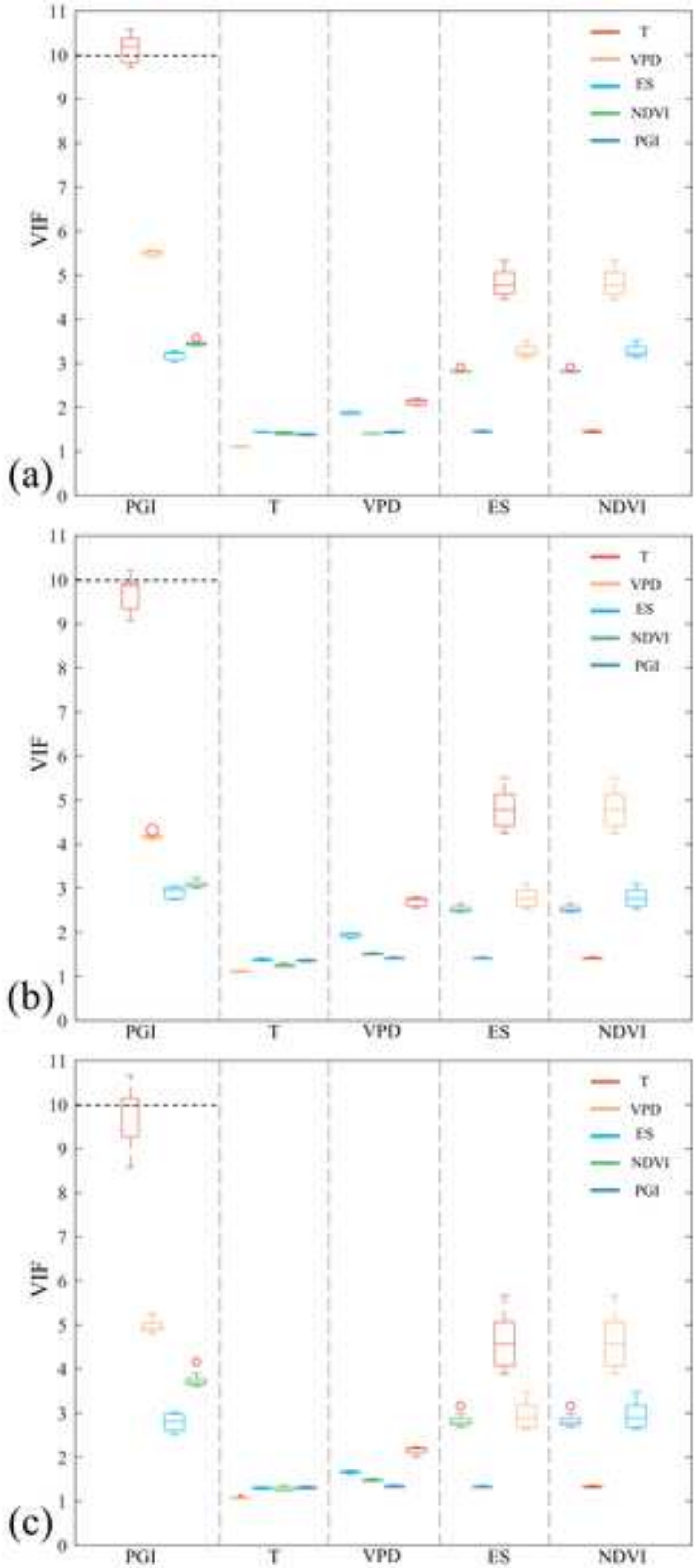

Figure S2

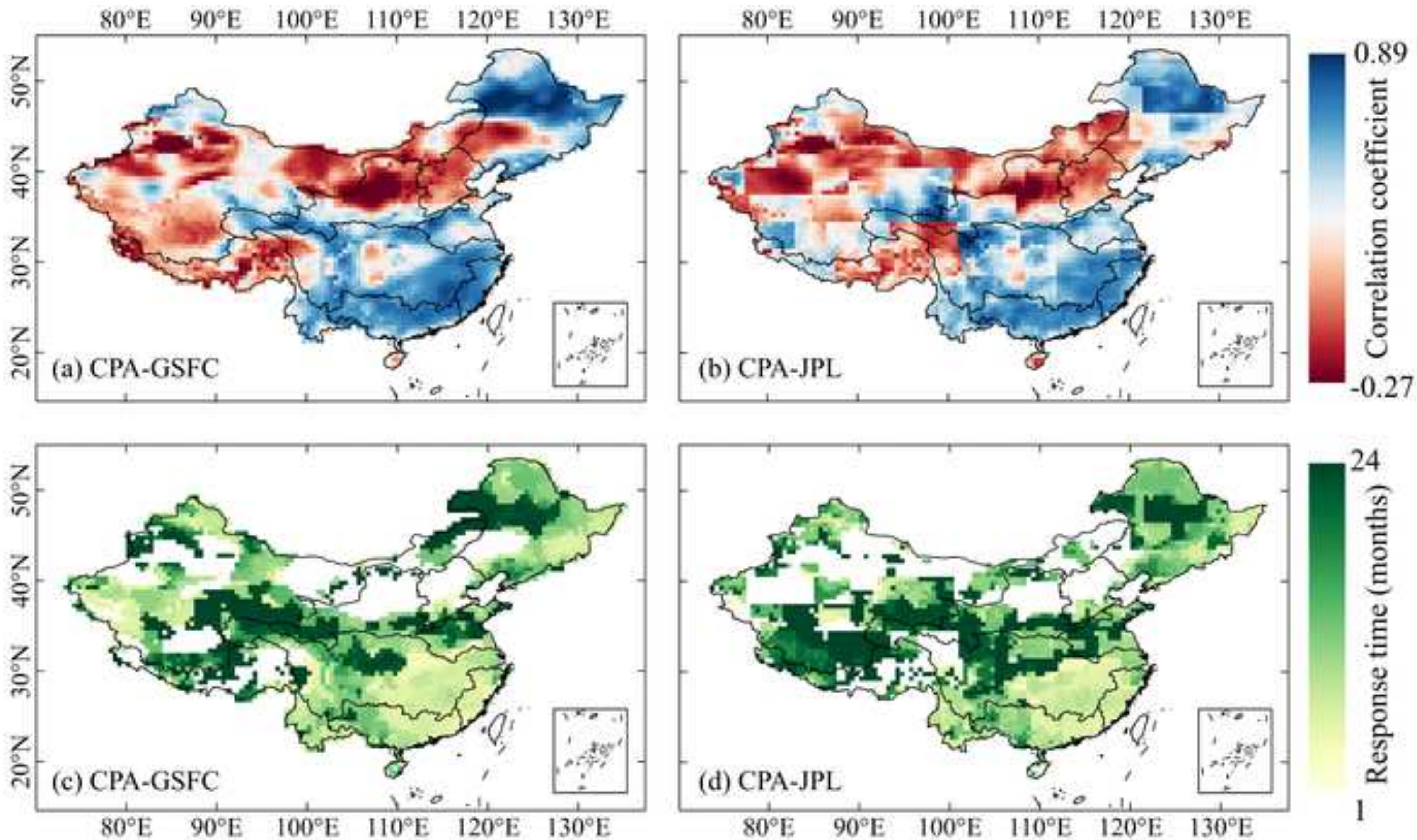
80°E
90°E
100°E
110°E
120°E
130°E
50°N
40°N
30°N
20°N
(a) CPA-GSFC
(b) CPA-JPL
(c) CPA-GSFC
(d) CPA-JPL
0.89
-0.27
Correlation coefficient
24
1
Response time (months)

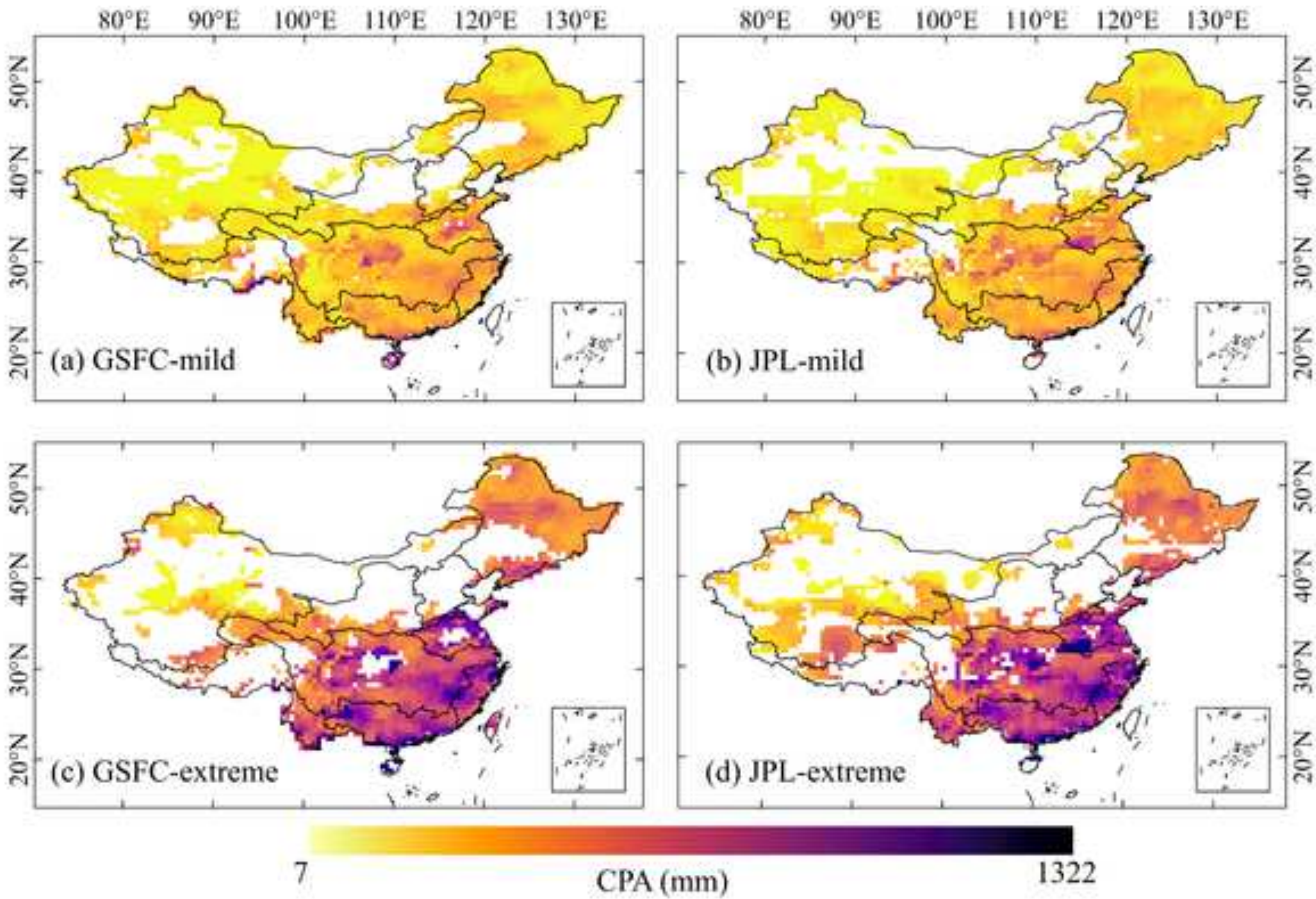
80°E
90°E
100°E
110°E
120°E
130°E
50°N
40°N
30°N
20°N
(a) GSFC-mild
(b) JPL-mild
(c) GSFC-extreme
(d) JPL-extreme
7
CPA (mm)
1322

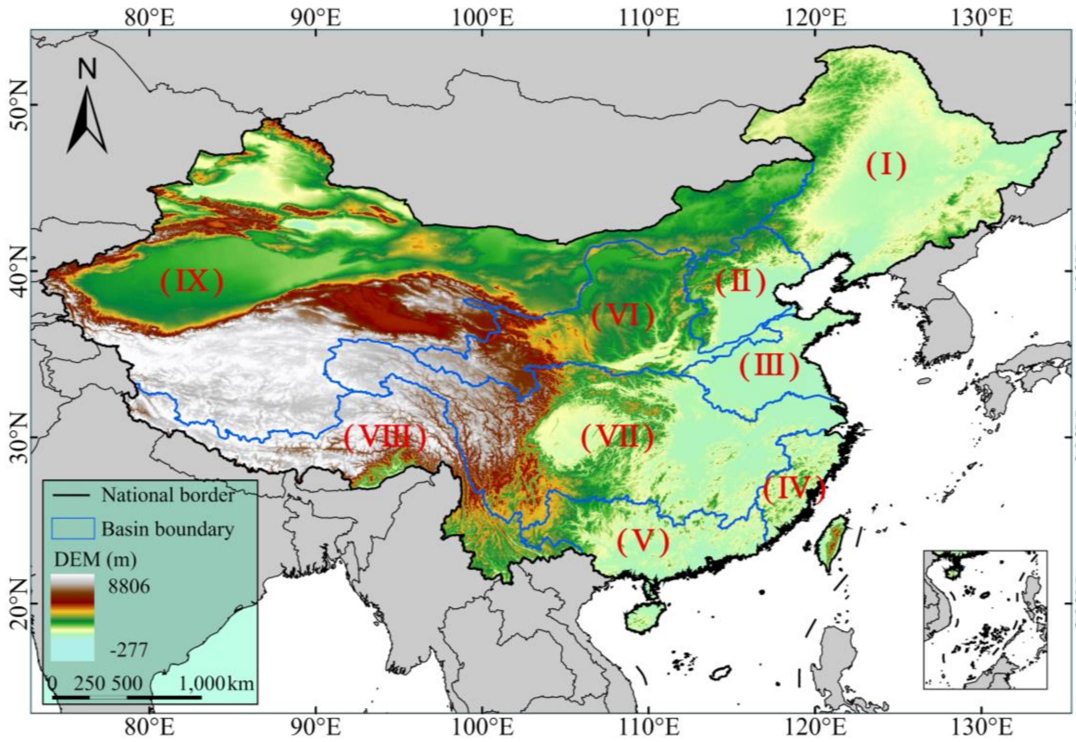

Fig. 1 Location map of the study area.

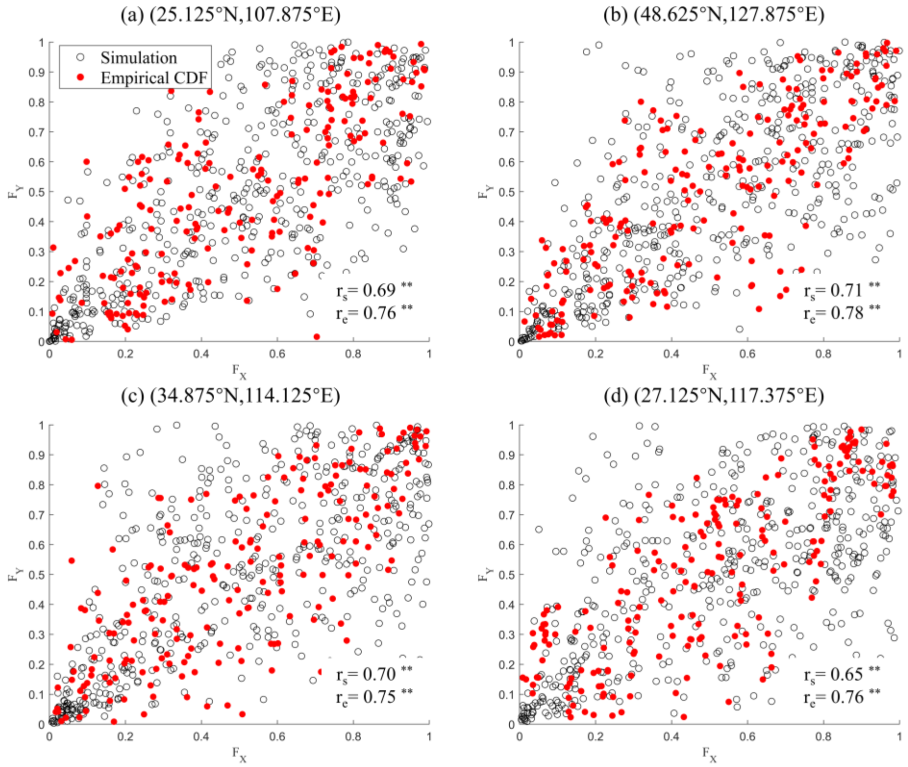

Fig. 2 The comparison between the observed combination of CPA and TWSA-DSI and the simulation of random variables using the Clayton copula function. The r_s and r_e are the correlation coefficient of simulations and observations, respectively. Note: "**" represents significance level of 0.01.

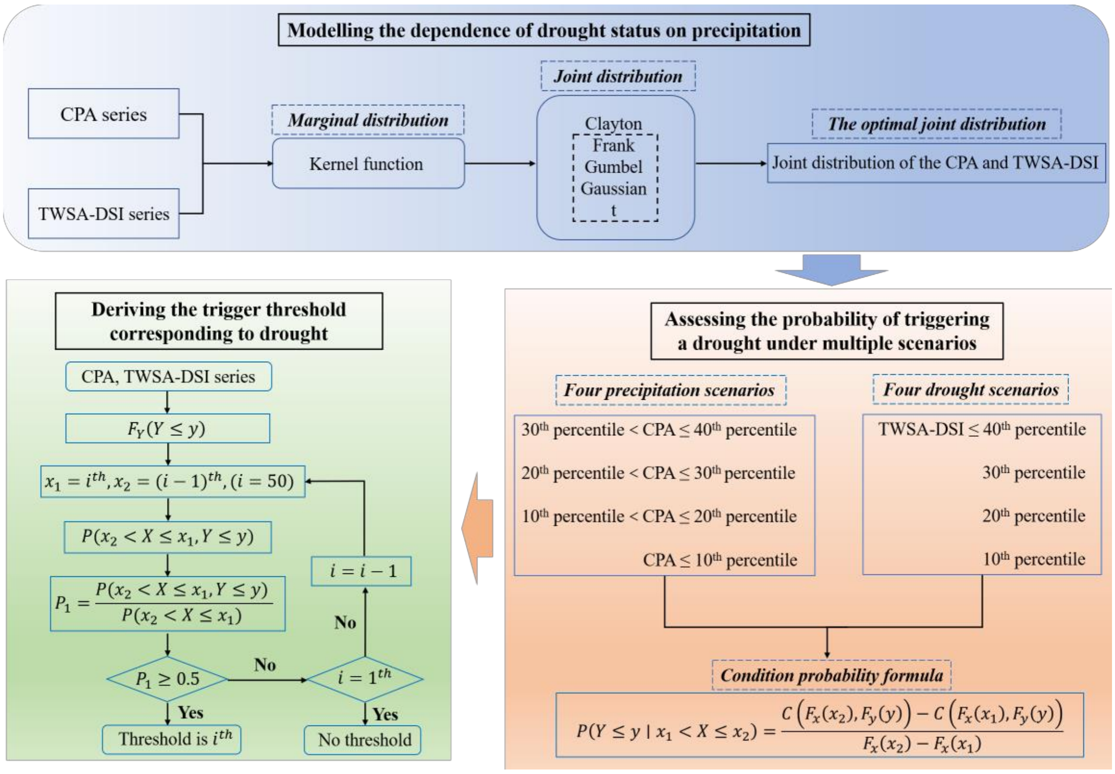

Fig. 3 Precipitation-driven drought trigger threshold framework.

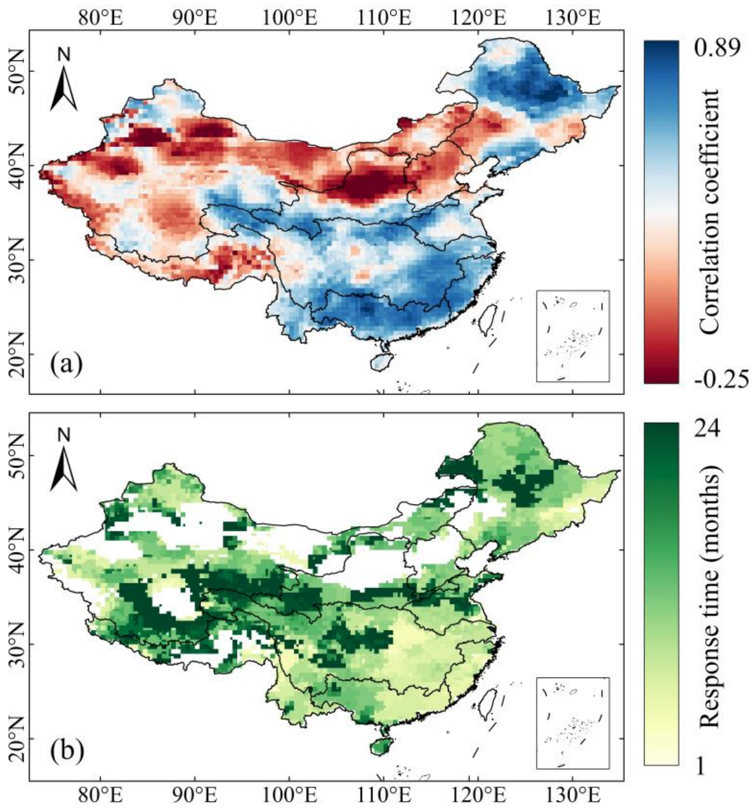

Fig. 4 Correlation between drought and precipitation (a) and its response time (b). The white pixels in (b) indicate the failure to pass the test for significant ($p<0.05$) positive correlation.

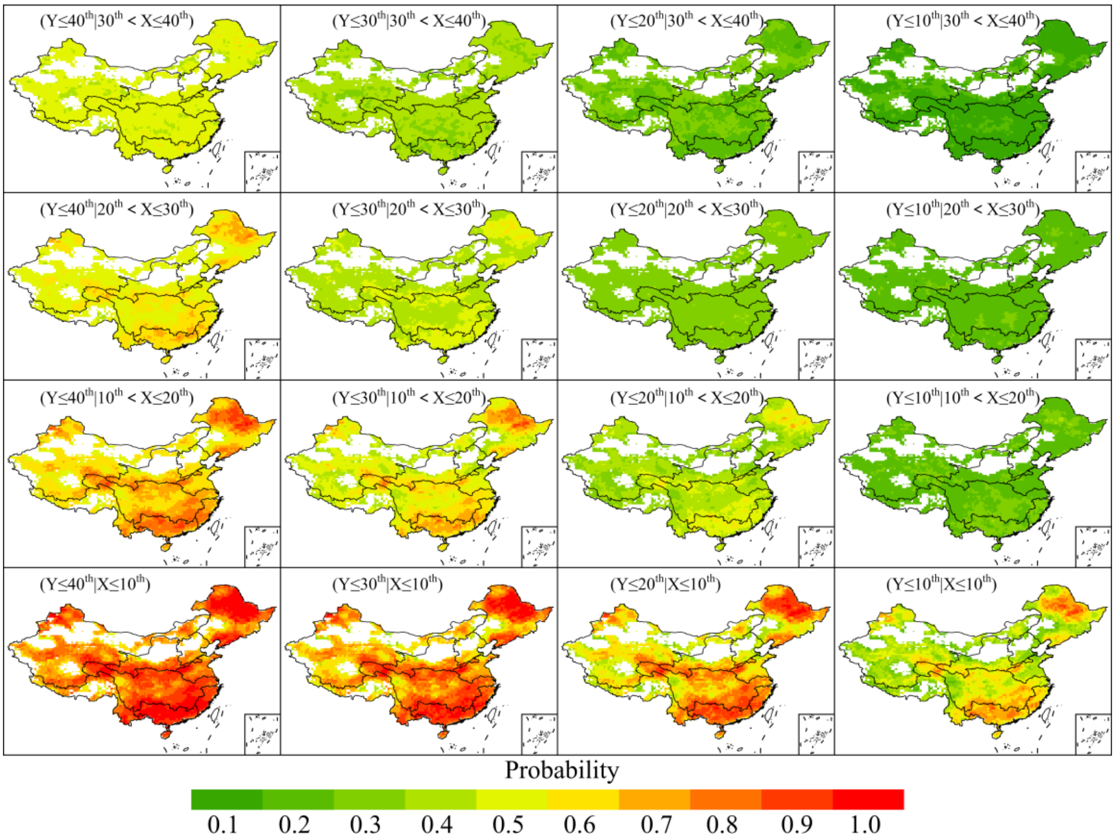

Fig. 5 Probability of triggering different levels (mild, moderate, severe and extreme) of drought given different percentile precipitation scenarios. The different CPA and TWSA-DSI scenarios are represented by X, Y in the panel.

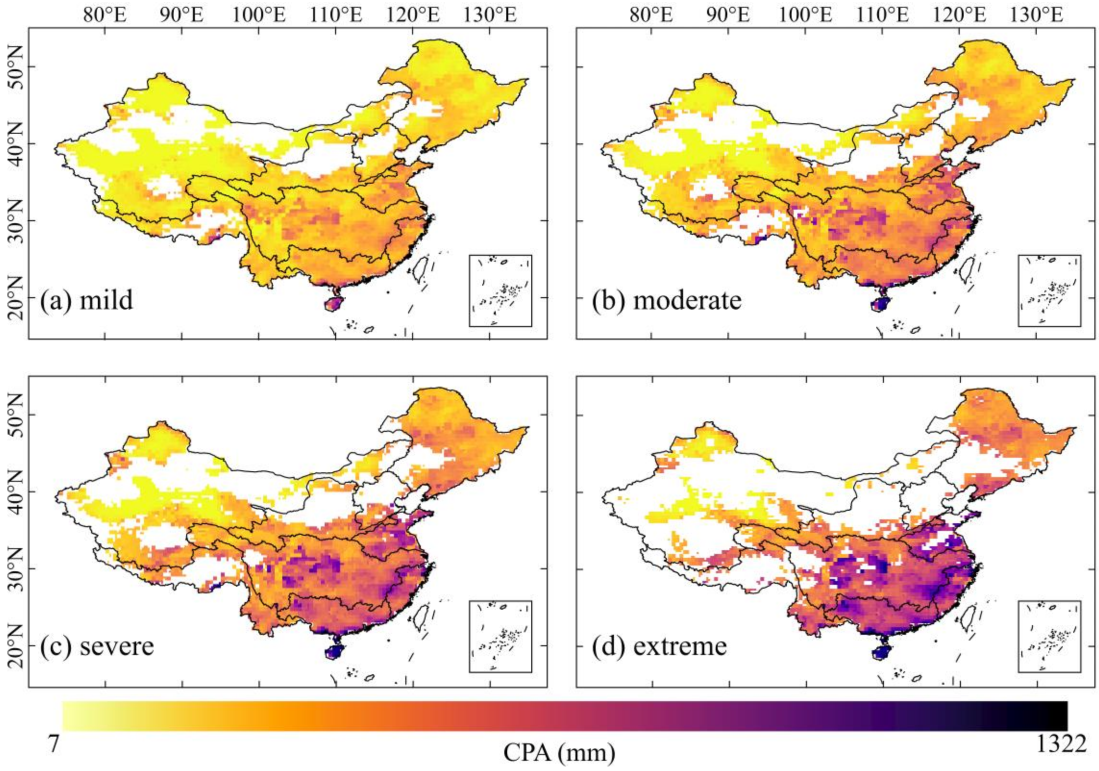

Fig. 6 The CPA corresponding to different levels of drought trigger thresholds. The white pixels in the panel indicate no threshold, and the same applies to subsequent figures.

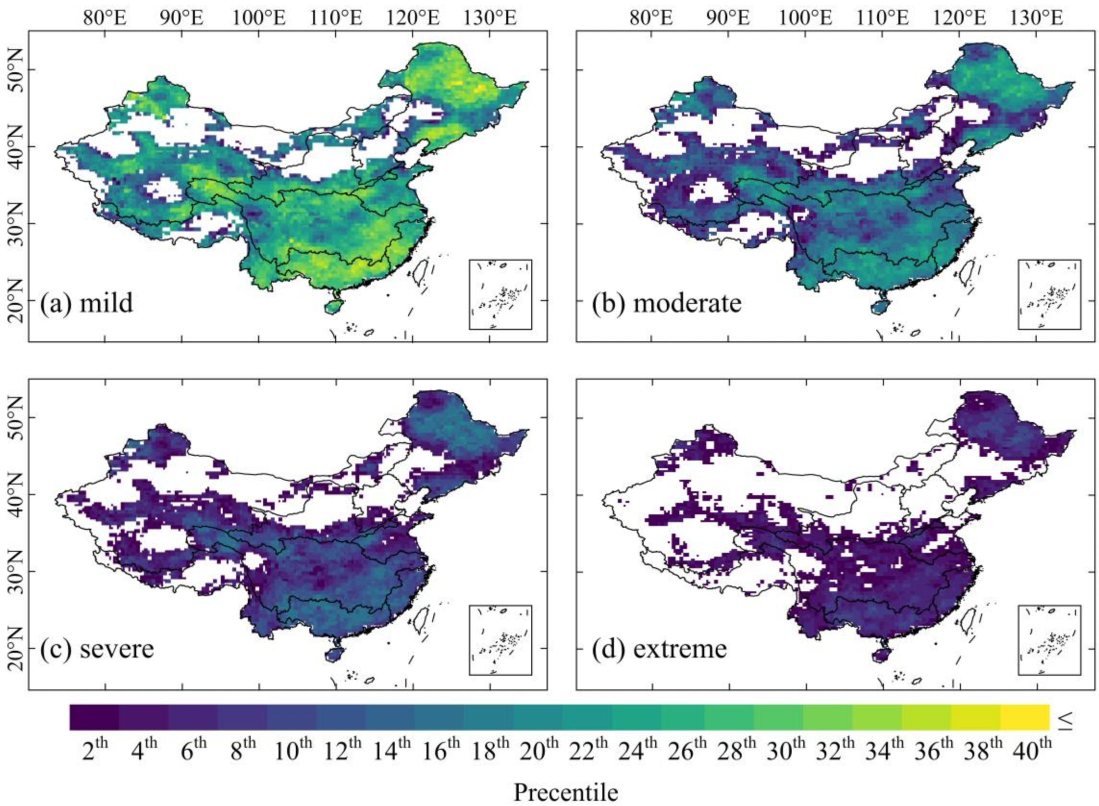

Fig. 7 The CPA percentile corresponding to different levels of drought trigger thresholds.

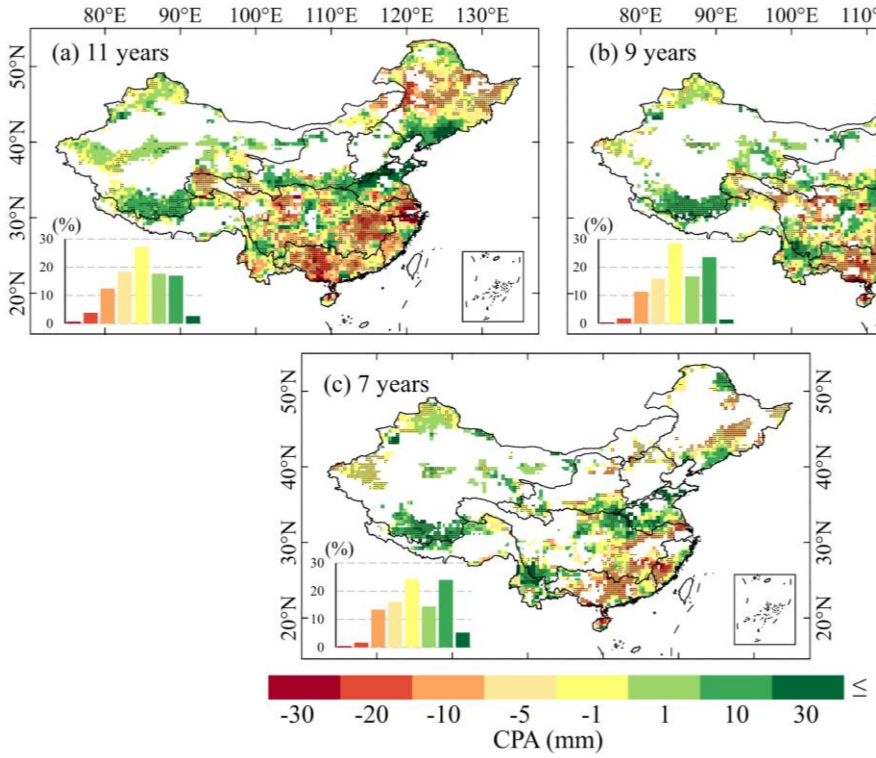

Fig. 8 Spatial trends in thresholds corresponding to mild drought under sliding windows of 11 (a), 9 (b), and 7 years (c), with black markers indicating significance at the 0.05 level. Histograms in panels show statistical proportions.

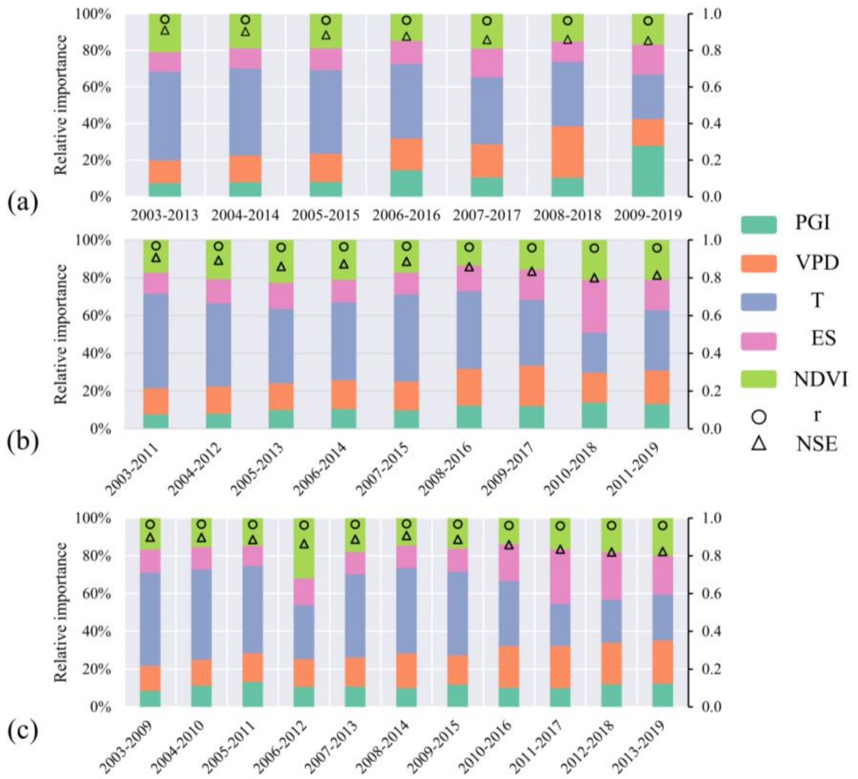

Fig. 9 The relative importance of various factors on triggering thresholds under sliding windows of 11 (a), 9 (b), and 7 years (c). Note: PGI, VPD, T, ES, NDVI, r and NSE represent population-GDP index, vapor pressure deficit, air temperature, evaporation flux from soil, normalized vegetation index, correlation coefficient and Nash-Sutcliffe efficiency respectively.

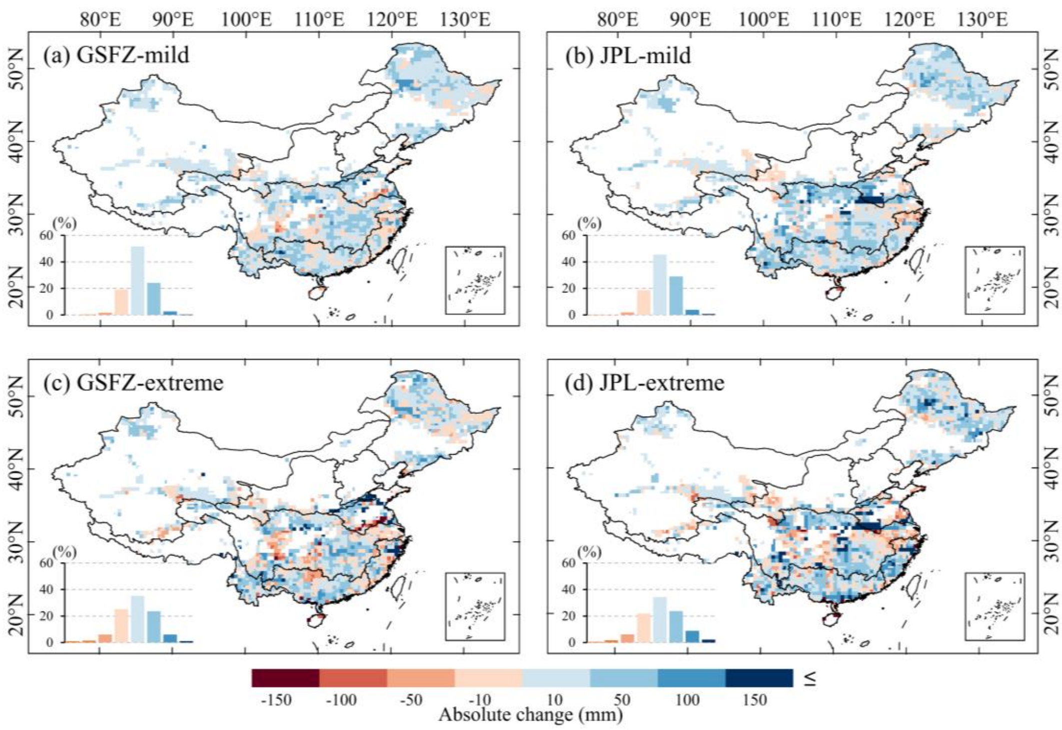

Fig. 10 Threshold changes in the GFSZ and JPL products for triggering mild drought, and their absolute differences from CSR products. Histograms in panels show statistical proportions.

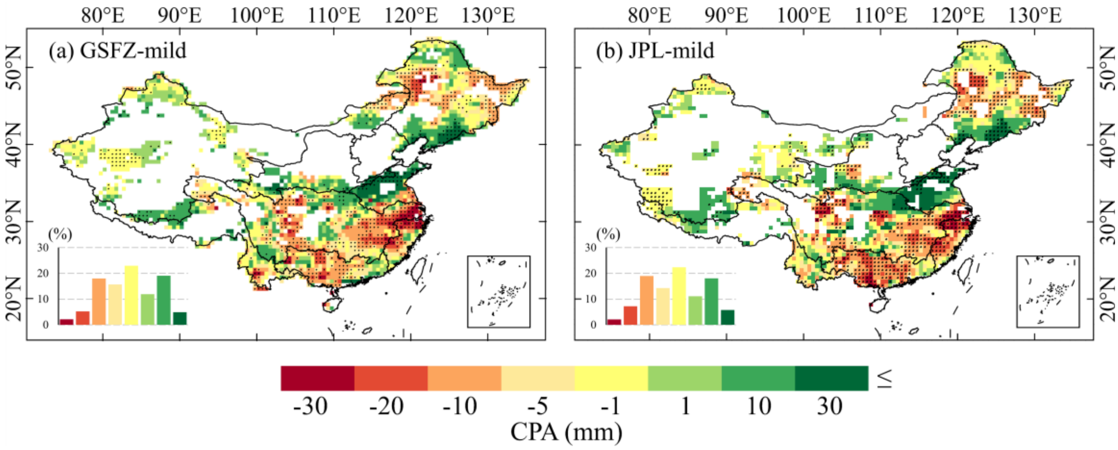

Fig. 11 Trends in thresholds for triggering mild drought for GFSZ and JPL products under an 11-year sliding window.

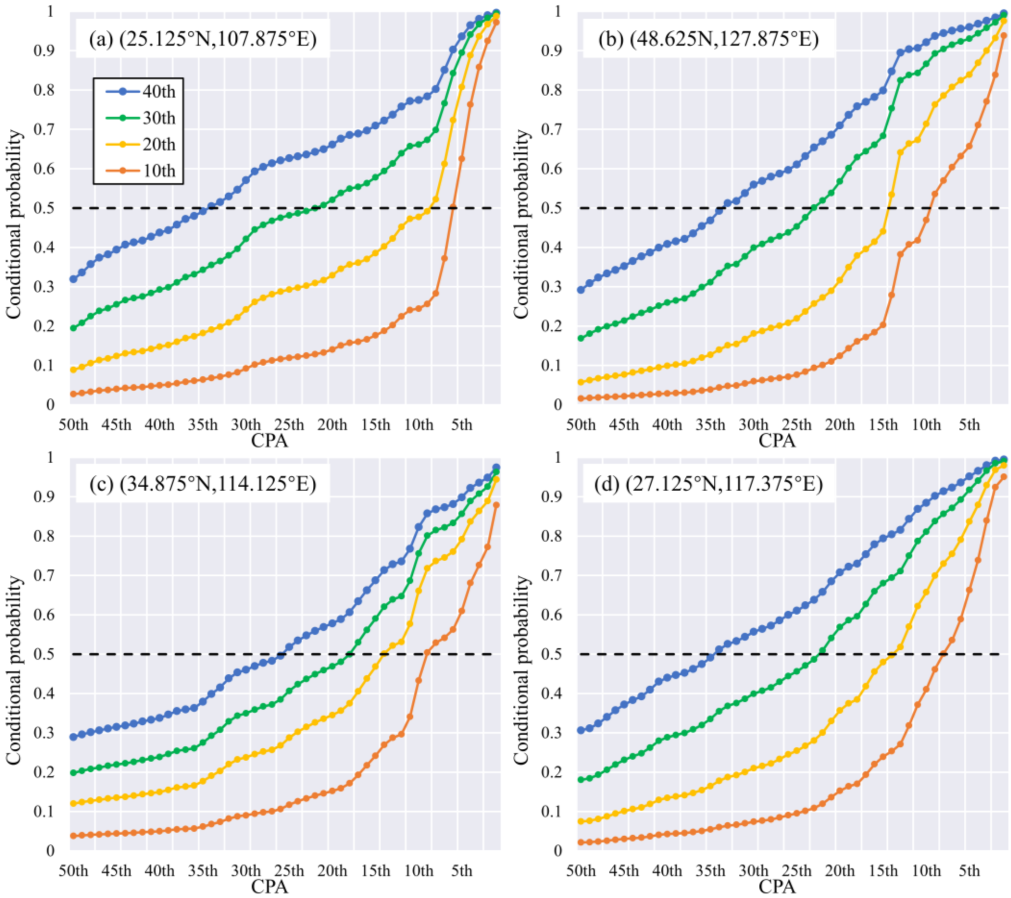

Fig. 12 Varying conditional probability of different CPA levels triggering different droughts in the four pixels, with the black dashed line indicating the set conditional probability.

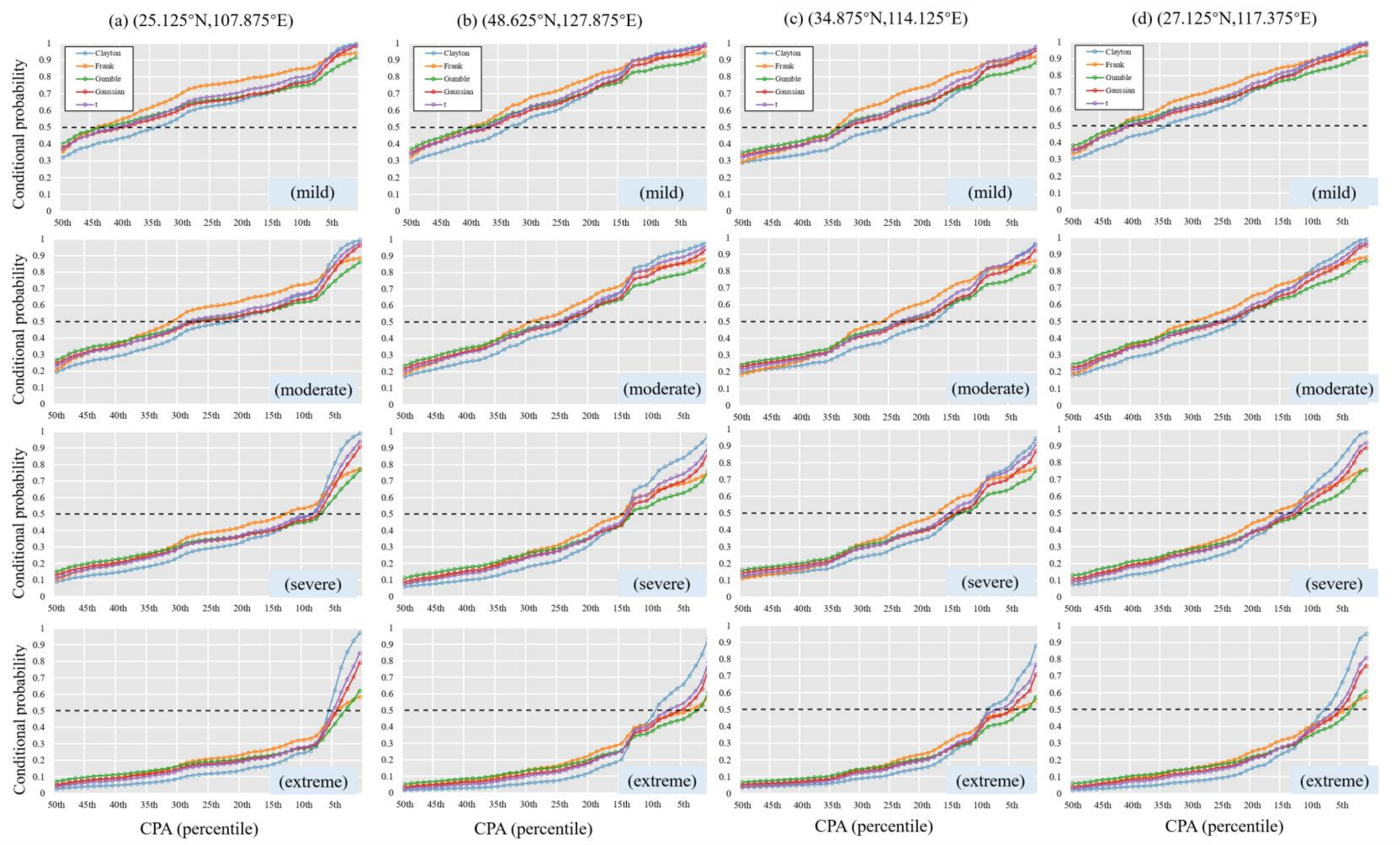

Fig. 13 The CPA based on different copula functions triggers changes in the conditional probability of different levels of drought, with the black dashed line indicating the set conditional probability

Supplementary materials

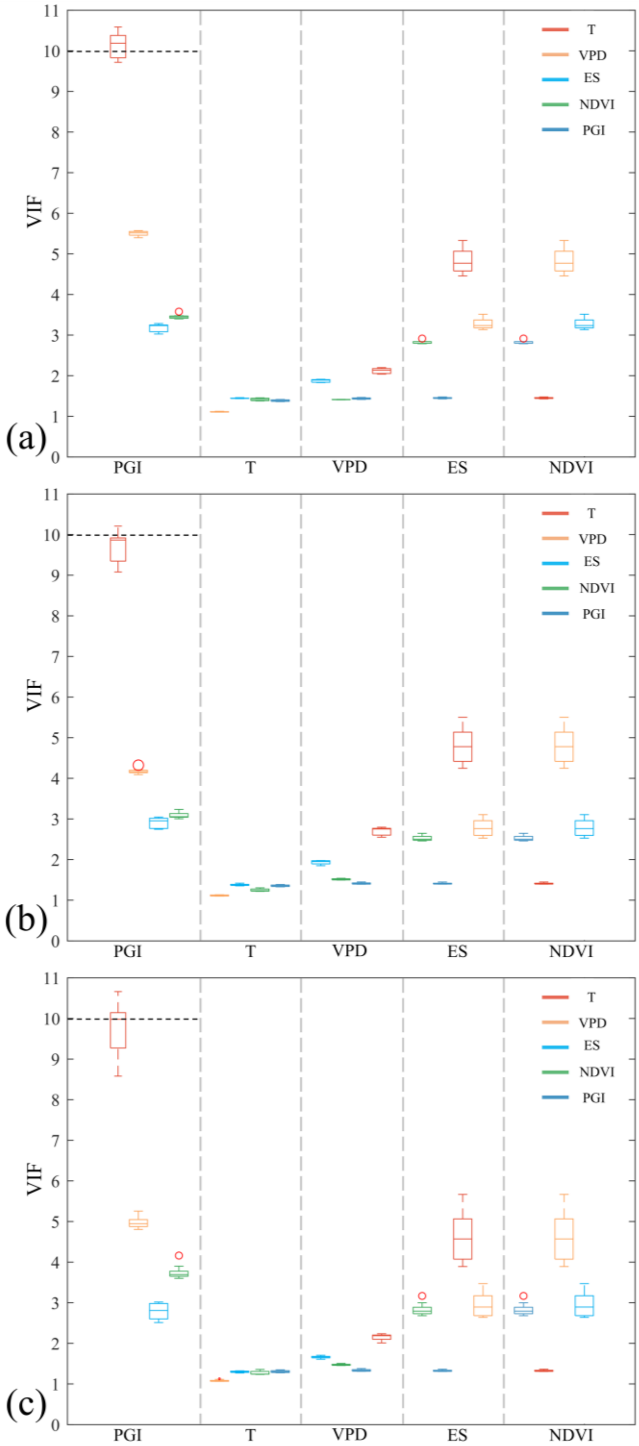

Fig. S1 Boxplot of the VIF variation between factors on sliding scale over 11 (a), 9 (b) and 7 years (c).

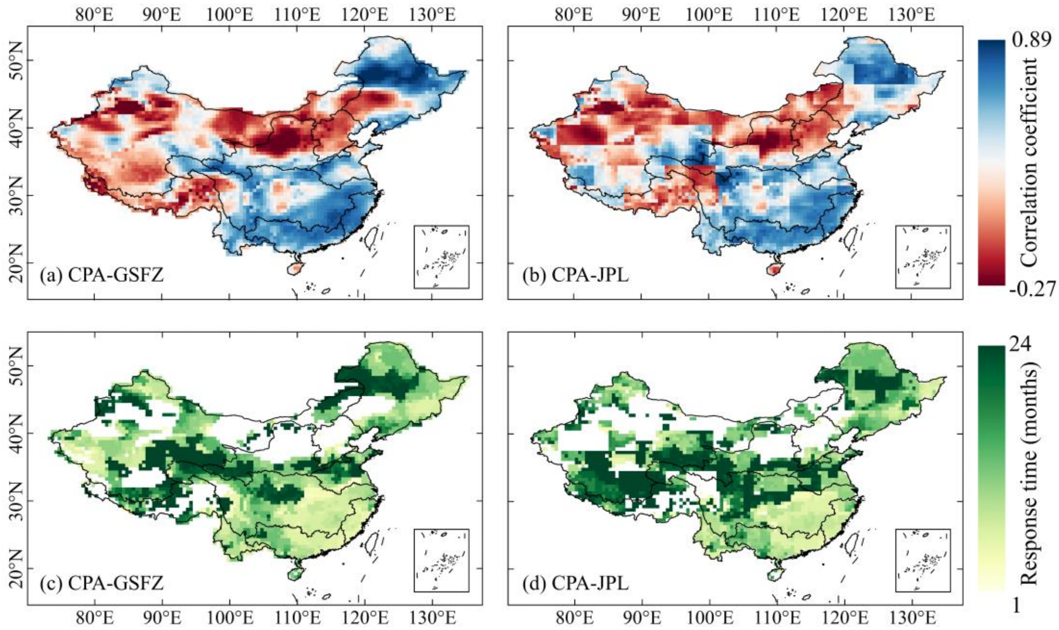

Fig. S2 Correlation of TWSA-DSI with CPA based on GSFZ and JPL products and their response time variation.

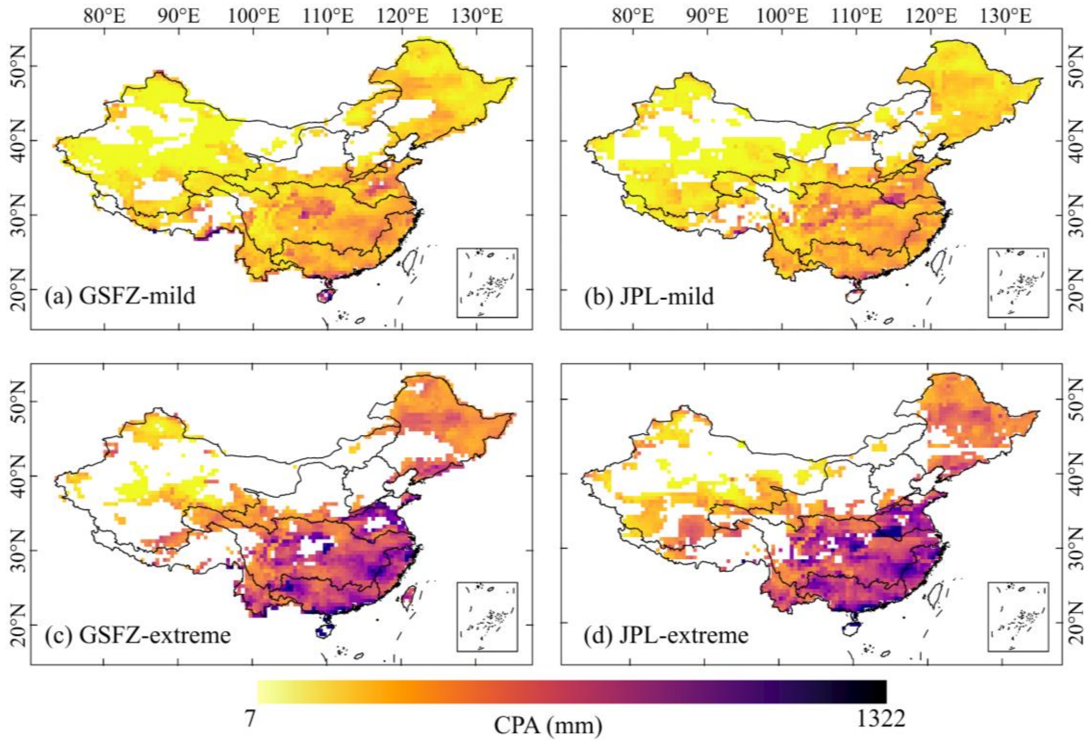

Fig. S3 Changes in CPA corresponding to triggered mild and extreme drought based on GSFZ and JPL products, respectively. White pixels in the panel indicate no threshold.